HU ISSN 2063-6792

# MATERIALS SCIENCE AND ENGINEERING

## A Publication of the University of Miskolc

Volume 38, Number 1 (2013)

**Miskolc University Press**
**2013**

**HU ISSN 2063-6792**

**Editors:** Dr. Ágnes Wopera
Gábor Nagy

# CONTENT

*Materials Science and Engineering, Volume 38/1. (2013), pp. 5–13.*

# STUDYING THE SPECTRAL INTERFERENCE EFFECTS OF ALUMINIUM EXPERIENCED IN THE COURSE OF ICP-AES ANALYSIS USING AN AXIALLY-VIEWED ICP SPECTROMETER

OLIVÉR BÁNHIDI[*]

Earlier we have reported the study of the interference effects of aluminium and nickel on the ion and atom lines of alkaline earth metal elements [1, 2]. According to our investigations strong interferences can be experienced especially on the Mg, Ca and Sr lines. The concentration of the alkaline-earth metal analyte tested ranged 0.25–0.75 mg/dm$^3$, which is rather low, but there might be samples, such as Sr in Al alloys, where this concentration range may be interesting too. On the other hand, there are many cases, when these elements are in a substantially higher concentration, so the information concerning the interferences of aluminium on the lines of the elements present in higher concentration also may be interesting. In this paper we report the study of the effect of aluminium matrix present in a concentration range of 0–5000 mg/dm$^3$, while the analyte concentration is in the range of 1–15 mg/dm$^3$.

**Keywords:** interference effects of aluminium, alkaline earth metals, ion and atom spectral lines.

## Introduction

In our previous papers we have investigated the effects of Al and Ni on the spectral lines of alkaline earth metals, such as Be, Mg, Ca and Sr. Both atom and ion lines were involved in the study. Ba was not among the analytes examined, as it does not have a sensitive atom line. In the course of the experiments it turned out, that both Al and Ni have larger interference effects on atom lines of the investigated elements than on those of ion lines. The effect was just significant in case of Be, and rather high impact could be measured on the lines of Mg, Ca, Sr. The phenomenon can be measured on a rather wide range of high-frequency power (900–1300 Ws). As for the concentration ranges, the matrix was present from 0 up to 5000 mg/dm$^3$, while the analyte concentration was 0.25–0.5 mg/dm$^3$, which is rather low, though there might be cases, e.g. Sr in aluminium alloys – when such low concentration – can also be interesting and important. Nevertheless it is also important to know, whether this effect works at higher analyte concentration, and if the answer is yes, how strong it can be. Therefore the study of the interferences of Al at higher analyte concentration was carried out. As one of our goals was to check whether the differences among the matrix effects on atom and ion lines persist at higher analyte concentration, therefore similarly to the previous work, both ion and atom lines were involved in the study.

---

[*] University of Miskolc, Institute of Chemistry
3515 Miskolc-Egyetemváros, Hungary
akmbo@uni-miskolc.hu

So that the present results could be compared to those measured earlier, we used the same procedure to evaluate the signals and to present the effects we experienced.

## 1. Experimental

### *1.1. The measuring instrument and the measuring conditions*

The measurements were carried out with the help of a Varian-make ICP spectrometer, its type is 720 ES, the instrument we used earlier. As for as the measuring conditions, there is an important difference, in this study the measurements were performed only just at one level of the radiofrequency power, 1050 W. The other parameters – integration time, number of readings etc. – were the same.

### *1.2. Line selection and the analyte elements*

*Table 1*

*The spectral lines chosen for the study*

| **Element** | **First ionisation energy** [eV] | **Type of the line** | **Wavelength** [nm] | **Excitation energy** [eV] |
|---|---|---|---|---|
| Mg | 7.6 | Mg II | 279.553 | 4.47 |
| | | Mg II | 280.270 | 4.59 |
| | | Mg I | 285.213 | 4.38 |
| Ca | 6.1 | Ca II | 315.887 | 3.96 |
| | | Ca II | 317.933 | 3.93 |
| | | Ca II | 393.366 | 3.18 |
| | | Ca I | 422.673 | 2.96 |
| Sr | 5.7 | Sr II | 216.596 | 5.78 |
| | | Sr II | 407.771 | 3.07 |
| | | Sr II | 421.552 | 2.96 |
| | | Sr I. | 460.733 | 2.71 |
| Ba | 5.2 | Ba II | 233.527 | 5.35 |
| | | Ba II | 455.403 | 2.74 |
| | | Ba II | 493.408 | 2.53 |
| | | Ba II | 614.171 | 2.04 |
| | | Ba I | 705.994 | 1.77 |

Our aim was to measure possibly all the alkaline-earth metals, so that the most comprehensive information could be obtained about the interference effects. On the other hand, a higher and wider concentration range was going to be applied regarding the analyte elements. This fact made difficult to include Be among the analytes studied, because its available atom and ion lines are rather sensitive, so it might have turned out that the CCD detector measuring some of its lines would have overflown at higher concentration, so the result could not have been evaluated. On the other hand, as a result of the higher concentration range it was possible to include Ba among the elements investigated. It was because at higher concentration suitable signal can be obtained even on the less sensitive lines. The lines selected for the study can be seen in Table 1.

### *1.3. Concentration of the Al-matrix and those of analyte elements*

As in the earlier studies the Al matrix was applied at a concentration of 0, 200, 500, 1000, 2000 and 5000 mg/dm$^3$. The solutions were prepared using 20 g/dm$^3$ Al stock solution made by dissolving high-purity aluminium.

The analyte elements, i.e. Mg, Ca, Sr, Ba, were applied at a concentration of 0, 1.0, 2.5, 6.2, and 15 mg/dm$^3$, so the concentration range is a bit more than 1 order of magnitude. 1000 mg/dm$^3$ multielement certified reference material solution (Certipure IV, made by Merck GmbH) was used in the experiments.

## 2. Results

### *2.1. Processing the measured intensity values*

The net intensities of the investigated alkaline-earth elements measured in the matrix element-free solutions were used as reference, i.e. the net intensities measured at different matrix element concentrations were compared to that of obtained in matrix-free solutions, and heir ratio (i.e. $I_{matrix}/I_{aqueous}$) was investigated as the function of matrix and analyte concentration.

*Table 2*

*The net intensities and intensity ratios measured on 3 Mg lines, at an analyte concentration of 1 mg/dm$^3$*

| Al [mg/dm$^3$] | Mg II, 279.553 nm | | Mg II, 280.270 nm | | Mg I, 285.213 nm | |
|---|---|---|---|---|---|---|
| | $I_{net}$ [a.u.] | $I_{ratio}$ | $I_{net}$ [a.u.] | $I_{ratio}$ | $I_{net}$ [a.u.] | $I_{ratio}$ |
| 0 | 578052 | – | 158925 | – | 77613 | – |
| 200 | 610412 | 1.0511 | 162167 | 1.0161 | 68669 | 0.8808 |
| 500 | 605225 | 1.0376 | 161792 | 1.0099 | 65831 | 0.8411 |
| 1000 | 600111 | 1.0329 | 160724 | 1.0075 | 62900 | 0.8066 |
| 2000 | 559443 | 0.9269 | 148433 | 0.8972 | 57094 | 0.7054 |
| 5000 | 565816 | 0.9611 | 149161 | 0.9252 | 56069 | 0.7100 |

As the number of the measured lines were high, a lot of intensity data had to be recorded.

The date were processed by a spreadsheet program. In Table 2 and Table the measured net intensities as well as the calculated intensity ratios ($I_{matrix}/I_{aqueous}$) of 3 Mg lines at an analyte concentration of 1.0 mg/dm$^3$ and that of 15 mg/dm$^3$ are presented.

*Table 3*

*The net intensities and intensity ratios measured on 3 Mg lines, at an analyte concentration of 15 mg/dm$^3$*

| C(Ni) [mg/dm$^3$] | Mg II, 279.553 nm | | Mg II, 280.270 nm | | Mg I, 285.213 nm | |
|---|---|---|---|---|---|---|
| | $I_{net}$ [a.u.] | $I_{ratio}$ | $I_{net}$ [a.u.] | $I_{ratio}$ | $I_{net}$ [a.u.] | $I_{ratio}$ |
| 0 | 7170830 | – | 2191330 | – | 1029450 | – |
| 200 | 7354630 | 1.0252 | 2160140 | 0.9855 | 1006270 | 0.9272 |
| 500 | 7058910 | 0.9836 | 2119780 | 0.9668 | 970603 | 0.9423 |
| 1000 | 6883420 | 0.9595 | 2049830 | 0.9351 | 922022 | 0.8954 |
| 2000 | 6674980 | 0.9276 | 1994580 | 0.9076 | 867083 | 0.8400 |
| 5000 | 9513880 | 1.3254 | 2957340 | 1.3486 | 1293330 | 1.2555 |

Similar tables were created for each line of all elements measured.

### 2.2. The Figures based upon the intensity ratios of the tables

Using the data in the tables different figures were created, where the intensity ratios measured on different lines of an analyte studied were presented as the function of the matrix concentration at a given concentration of one of the analytes investigated. In Figure 1, 2 the intensity ratios of Mg lines can be seen at the lowest and the highest analyte concentration, while in Figure 3 and 4 the same is presented in case of Ca and the strontium data can be seen in Figure 5 and 6.

### 2.3. Calculation the relative difference of the intensity ratios of atom and ion lines

Looking at these figures it can be seen that the intensity ratios of the atomic lines of the elements studied are always lower than that of the ion lines in case of each elements. The difference is usually higher at higher concentration of the interfering element.

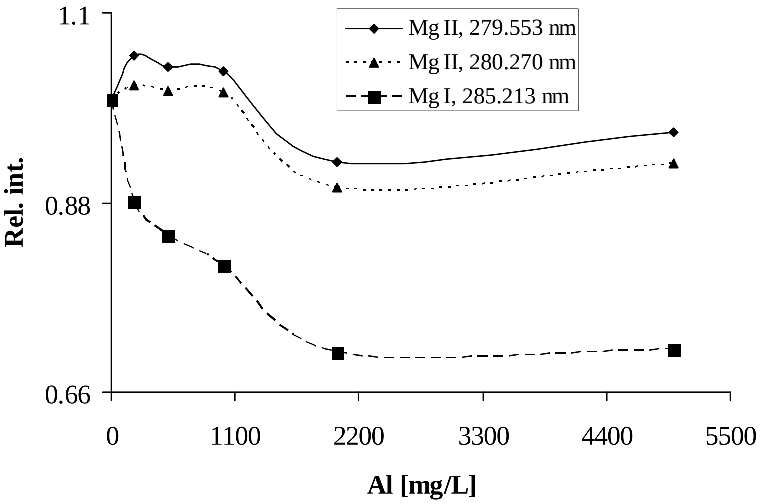

*Figure 1. Intensity ratios measured on the Mg lines, at an Mg concentration of 1 mg/dm*$^3$

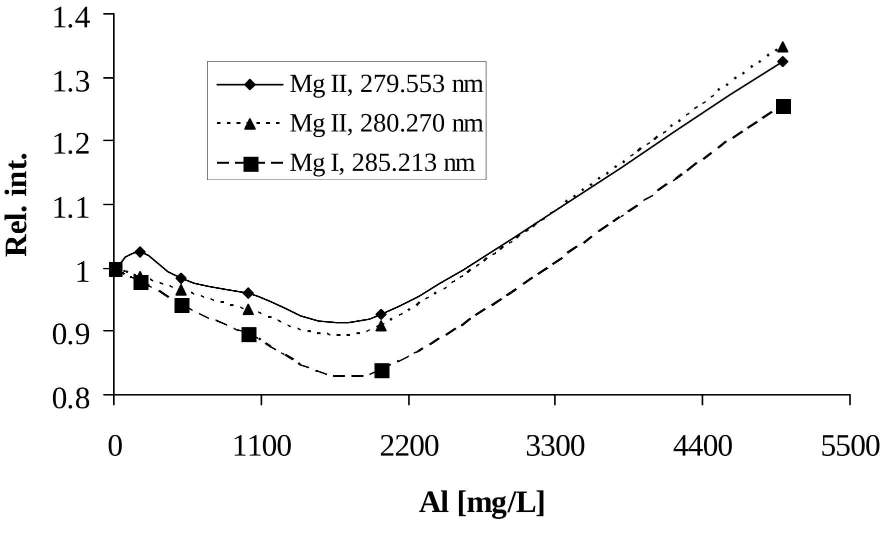

*Figure 2. Intensity ratios measured on the Mg lines, at an Mg concentration of 15 mg/dm*$^3$

*Table 4*

*The lines chosen for calculating the relative intensity reduction of the atom lines of the element studied*

| **Element** | Mg | Ca | Sr | Ba |
|---|---|---|---|---|
| Atomic line [nm] | 279.553 | 422.673 | 460.733 | 705.994 |
| Ion line [nm] | 285.213 | 317.933 | 216.596 | 233.527 |

In Table 4 this reduction is presented for each element in form of relative %. The calculation is based upon the following formula:

$$\textbf{Difference [rel. \%]} = 100*(I_{Rion} - I_{Ratom})/I_{Rion}$$

Where $I_{Rion}$ is the intensity ratio of the ion line and $I_{Ratom}$ is the intensity ration of the atom line. For the calculation the intensity ratio of one ion line and that of the atomic line of each element were used. The lines used in the calculation are indicated in Table 5.

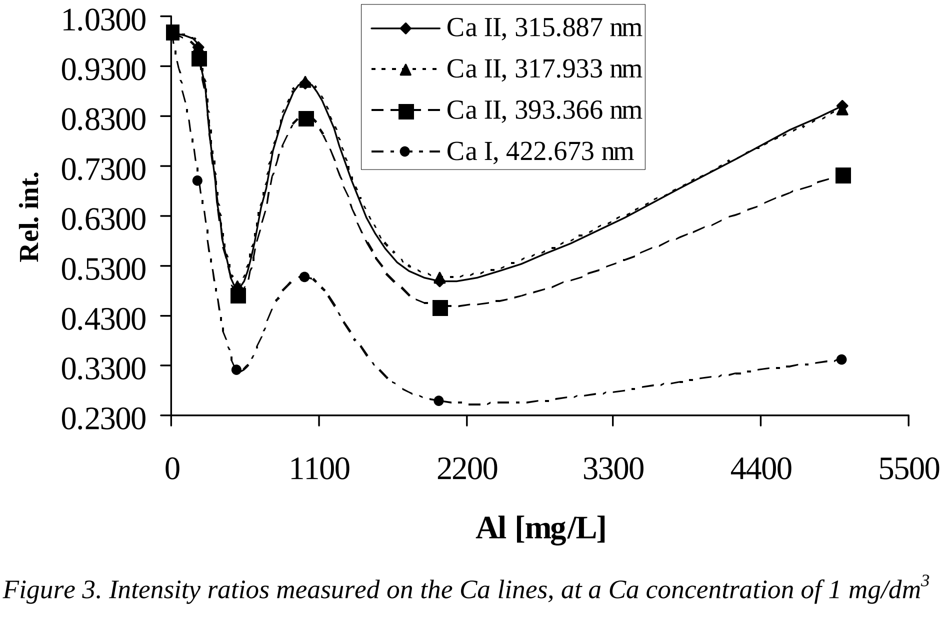

*Figure 3. Intensity ratios measured on the Ca lines, at a Ca concentration of 1 mg/dm$^3$*

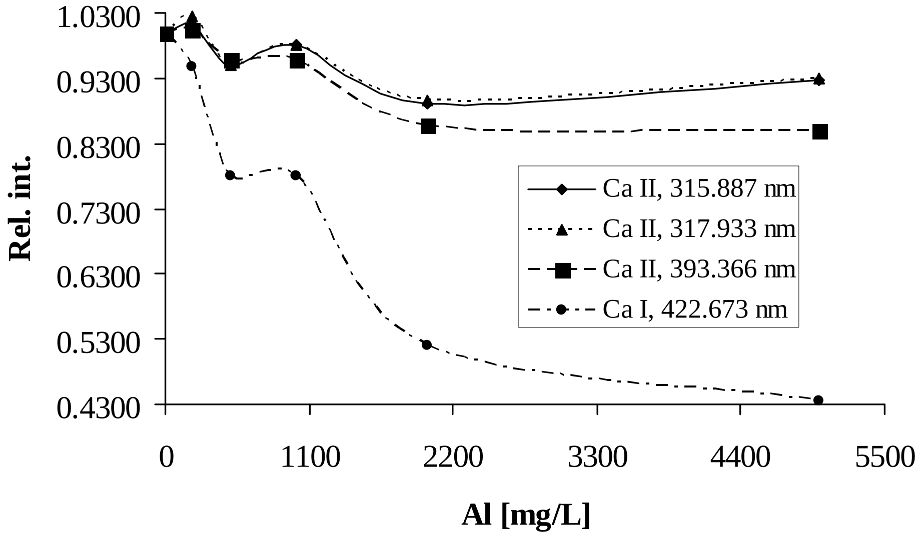

*Figure 4. Intensity ratios measured on the Ca lines, at a Ca concentration of 15 mg/dm$^3$*

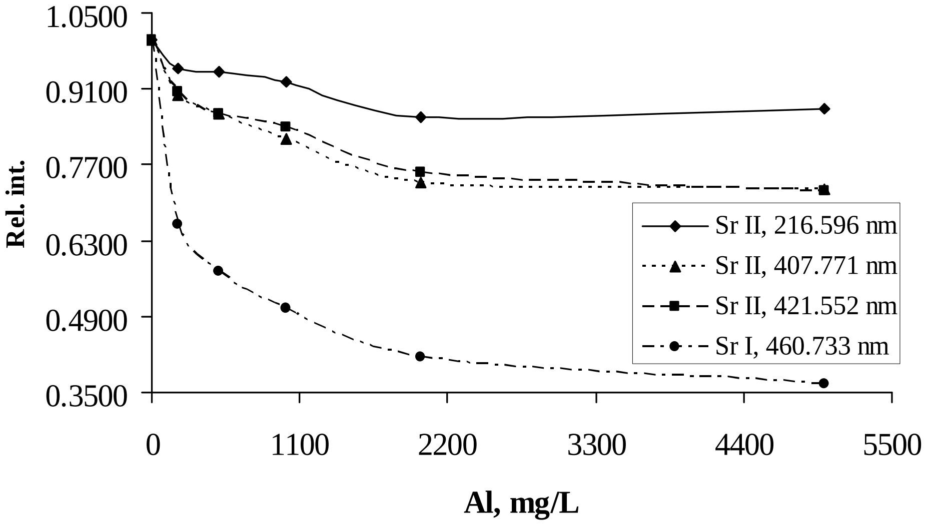

*Figure 5. Intensity ratios measured on the Sr lines, at a strontium concentration of 1 mg/dm$^3$*

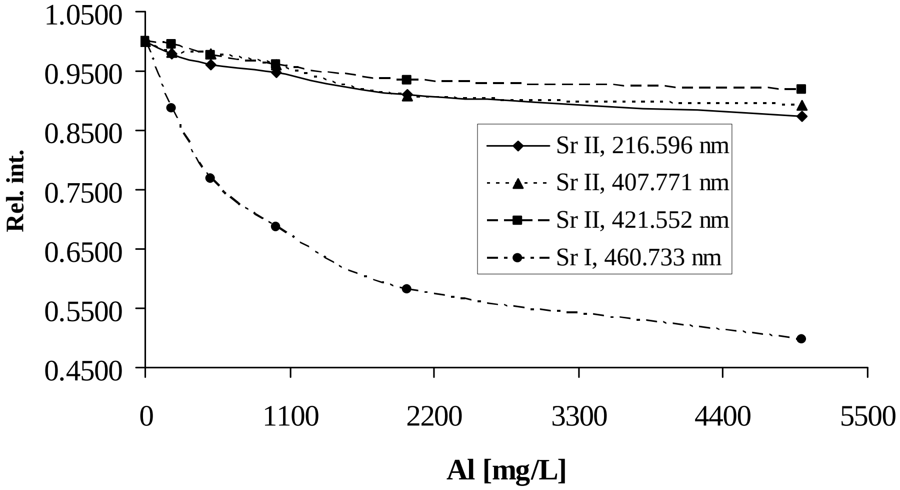

*Figure 6. Intensity ratios measured on the Sr lines, at a strontium concentration of 15 mg/dm*$^3$

*Table 5*

*The relative intensity ratio difference between an atom and an ion line at low and high concentration of the Al matrix, as a function of the analyte concentration*

| **Element** | **Analyte concentration** | | | | | | | |
|---|---|---|---|---|---|---|---|---|
| | 1 mg/dm$^3$ | | 2.5 mg/dm$^3$ | | 6.2 mg/dm$^3$ | | 15 mg/dm$^3$ | |
| | Al [mg/dm$^3$] | | Al [mg/dm$^3$] | | Al [mg/dm$^3$] | | Al [mg/dm$^3$] | |
| | 200 | 5000 | 200 | 5000 | 200 | 5000 | 200 | 5000 |
| Mg | 16.20 | 26.13 | 10.35 | 20.84 | 6.57 | 16.13 | 4.69 | 5.27 |
| Ca | 27.57 | 59.54 | 20.47 | 56.20 | 13.57 | 50.52 | 7.72 | 53.36 |
| Sr | 30.45 | 58.16 | 20.41 | 53.64 | 13.79 | 45.16 | 9.53 | 43.01 |
| Ba | 51.72 | 48.50 | 24.47 | 40.02 | 11.34 | 21.68 | 2.73 | 10.34 |

## 3. Discussion of the results

Axially viewed ICP spectrometers are said to produce more interferences than those of radial viewed instruments, therefore care must be taken of the examination of possible interferences in the course of method development. As it can be seen there may be strong differences concerning the extent of the interferences on the different type of spectral lines. In most cases the intensity of the spectral lines was lower in the presence of aluminium, than in the aluminium-free solution. Looking at the curves in all the 6 Figures it is obvious that in all cases the line intensity decreased in the presence of matrix in greater extent on atom lines than on ion lines. It also can be noticed that except for the Mg lines at high analyte concentration the difference increases with increasing matrix concentration. If the intensity ratios, i.e. the relative intensity referred to the signal measured in the aluminium-free solution are examined as the function of the analyte concentration and that of the matrix concentration, the relative difference between an ion and an atom line may also be interesting. When looking at the data presented in Table 5, it can be realized that the difference between the behaviour of the ion and atom lines studied depends not only on the matrix concentration and that of the analyte concentration but also on the element examined. While at low analyte concentration (1 mg/dm$^3$) there is a substantial difference among the ratios in all elements both at low and high matrix concentration, the behaviour of the lines changes at high analyte concentration, and this change is different for each element. At low analyte concentration a strong reduction of the differences can be noticed for all elements, but at high analyte level (15 mg/dm$^3$) the reduction in the difference depends largely on the elements. In case of Mg and Ba the reduction is high, while the differences decrease only in a moderate extent on Ca and Sr lines.

## Conclusions

As for the analytical practice these results support the importance of matrix-matching [3] and suggest that careful line selection and study of the possible interferences have key-importance when atom-emission methods are developed so that correct analytical results could be obtained when new type of matrix is to be analysed.

### Acknowledgement

*The described work was carried out as part of the TÁMOP-4.2.1.B-10/2/KONV-2010-0001 project in the framework of the New Hungarian Development Plan. The realization of this project is supported by the European Union, co-financed by the European Social Fund.*

### References

[1] Bánhidi, O.: *Examination of the Interference Effects on the Course of ICP-AES Determination of Strontium Content of Aluminium Alloys*. XXVI microCAD University of Miskolc, 29–30 March 2012 Section C, CD-issue of the Conference Publications
[2] Bánhidi, O.: *Material Science Forum, under publication*
[3] Záray, Gy. (ed.): *Az elemanalitika korszerű módszerei*. (In rough translation: Modern Methods of Elementary Analytics.) Akadémiai Kiadó, Budapest, 2006.

*Materials Science and Engineering, Volume 38/1. (2013), pp. 15–27.*

# INFLUENCE OF THE SHORT TIME GRINDING ON THE THERMAL DECOMPOSITION PROCESSES OF GIBBSITE PRODUCED BY THE BAYER PROCESS

VIKTOR ZSOLT BARANYAI[1]–FERENC KRISTÁLY[2]–ISTVÁN SZŰCS[3]

The thermal decomposition of aluminum hydroxides follows two courses depending on the circumstances of the heat treatment (temperature, heating rate, pressure, etc.) and the properties of the particles (particle size, shape etc.). The conversion of aluminum hydroxides to aluminum oxides can occur via monohydroxide boehmite [$\gamma$ – AlO(OH)], or directly to oxides. In practice both courses exist, with the dominant decomposition of hydroxides directly to oxides.

We reduced the particle size of gibbsite [$\gamma$ – $Al(OH)_3$] produced by the Bayer process, by grinding to reduce the thermal decomposition via boehmite. Our aim was to avoid the conversion of the mineral composition of the aluminum hydroxides during the grinding. We examined the particle size, mineral composition via X-ray diffraction (XRD), and the thermal decomposition processes via thermogravimetry (TG) and differential thermal analysis (DTA) of the samples.

**Keywords:** gibbsite, thermal decomposition, grinding.

## Introduction

The end-product of the Bayer cycle, the gibbsite [$\gamma$ – $Al(OH)_3$] is calcined (thermally treated) to alumina (aluminum oxide). During the calcination he wet gibbsite loses first its adhesive moisture than the bonded water (34% referring to the dry hydrate material) exits. The only thermodynamically stable oxide phase is the corundum ($\alpha$-$Al_2O_3$). All of decomposition pathways are closed by the formation of corundum [1].

The pathway and degree of the decomposition of the aluminum-hydroxides are influenced by many factors, these are: the physicochemical properties of the initial raw (untreated) material (particle size, shape, substituting elements etc.) and the circumstances of the heat treatment (temperature, heating rate, composition of the atmosphere, pressure etc.) [2].

Several researchers investigated profoundly the processes of the calcination of aluminum-hydroxides. 0 schematically summarizes the pathways of gibbsite thermal decomposition. The following mechanisms are proposed in normal atmospheric air

---

[1] University of Miskolc, Department of Combustion Technology and Thermal Energy
3515 Miskolc-Egyetemváros, Hungary
tuzbvzs@uni-miskolc.hu

[2] University of Miskolc, Department of Mineralogy and Petrology
3515 Miskolc-Egyetemváros, Hungary
askkf@uni-miskolc.hu

[3] University of Miskolc, Department of Combustion Technology and Thermal Energy
3515 Miskolc-Egyetemváros, Hungary
tuzsi@uni-miskolc.hu

pressure. Gibbsite decomposes to oxide above the temperature of 300 °C. Increasing the temperature different transition alumina phases appear, further between 1150–1200 °C corundum evolves. Over 200 °C gibbsite loses two moles water transformed into oxi-hydroxide boehmite. Boehmite decomposes into transitional alumina at 500 °C. The last step of the pathway is the formation of corundum at 1050–1100 °C [1].

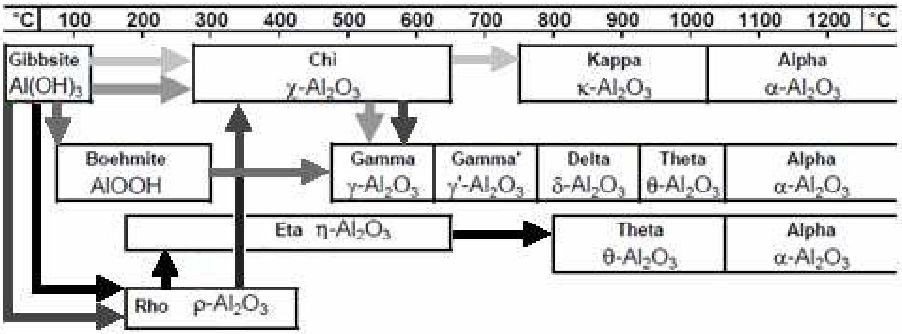

*Figure 1. The decomposition pathways of gibbsite [3]*

The formation of boehmite is the result of the hydrothermal processes within the particle. The conditions causing higher internal steam pressure within the particle (big particles, fast heating) favour the second pathway. While the heating is slow, small particles undergo direct decomposition into oxides [4].

Above statements are valid in case of calcintation at normal atmospheric pressure, while in case of vacuum or overpressure the decomposition processes are different [5]. According to experience both of the pathways exist when gibbsite from the industrial Bayer process is calcined. Wittmann et al. argued that the mass loss during the gibbsite-boehmite and the gibbsite-oxide conversion (up to 450 °C) is 28% while during the decomposition of the formed boehmite is 6.5%. Therefore the water molar ratio of the material, consisting of aluminum oxide and boehmite, became 0.57 after the gibbsite has been completely decomposed [6].

Long term grinding causes the transformation of the gibbsite into amorphous phases; the forming of gel-like hydroxides retains the initial water content of gibbsite. The dehydration of gel-like hydroxides begins at lower temperature and comprises a broader temperature interval compared to the dehydroxylation of gibbsite. The products of the dehydration of the gel-like hydroxides are amorphous oxides. The amorphous oxides transform at elevated temperatures into crystalline transitional oxides and further into corundum.

MacKenzie et al. argued that dehydration of gibbsite, if ground for 20 hours, is endothermic and occurs in two steps. At the temperatures 820 °C and 990 °C the endothermic reactions of formation of the crystalline phases are perceptible [7]. Koga reported that bayerite [$\beta - Al(OH)_3$], ground 30 hours, decomposes similarly. Grinding transforms the material into amorphous state; the thermal decomposition begins at lower temperature and occurs in a wider temperature range. The formed oxides are converted into crystalline form at 800 °C during exothermic reactions [8, 9].

Genc investigated the thermal conversion of ultrasonic treated boehmite samples. The decomposition of treated samples began at lower temperature [10]. The research results of thermal conversion of long term ground materials are utilizable in the ceramic industry [11]. The aim of our experiments was to find a short term grinding method, while the original mineral composition is kept unchanged, where the contribution of the pathway of thermal decomposition via boehmite declines. That gives us the possibility of avoiding the intruder effect of gibbsite-boehmite transformation in case of thermoanalytical investigation of samples containing mixture of aluminum-oxides-hydroxides and oxi-hydroxides.

## 1. Materials and experimental methods

### *1.1. Mechanical grinding*

The particle size distribution of the sample obtained from the bayer process is shown in 0. The aluminum hydroxide content of the sample is above 99.5% while the loss of ignition 34.5% is corresponding to the stoichiometric values. The samples were ground at a rotation speed of 500 rpm in an agate jar of 250 ml together with six agate balls of 18 mm in diameter. We used a Fritsch Pulverisette 6 planetary mill for different durations of grinding. The amounts of samples measured into the grinding jar were 24 or 6 g. The variable conditions of grinding are shown in Table 1. In cases of grinding times above five minutes we stopped the mill to scrape the material from the balls and the jar. The particle size distributions are shown in 0 and 4. The investigation of particle size was carried out in the presence of a sodium pyrophosphate solution and the samples were treated with ultrasound for one minute before the measurement.

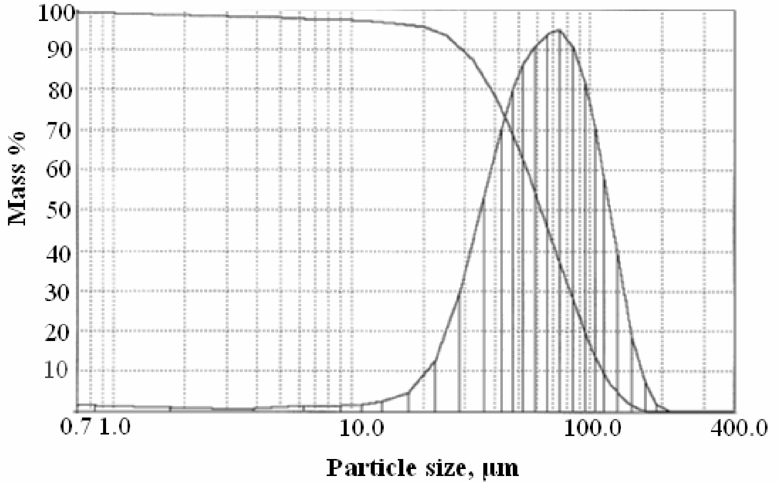

*Figure 2. Particle size distribution of the original sample*

*Table 1*

*The masses and grinding times of the different ground samples*

| **Sample number** | **1** | **2** | **3** | **4** | **5** |
|---|---|---|---|---|---|
| Ground sample mass, g | 24 | 24 | 24 | 6 | 6 |
| Grinding time, min | 1 | 5 | 10 | 10 | 15 |

The particle size of the sample that was ground for one minute doesn't show significant differences compared to the original unground sample, whereas in the case of samples 3 to 5 the particle size decreased by one order of magnitude. The duration of grinding is the same in the case of samples 3 and 4, only the amounts poured into the grinding jar differ. It is observable that the effect of the amount of ground material on the formed particle size is not significant. The finest sample is the aluminum hydroxide ground 15 minutes long.

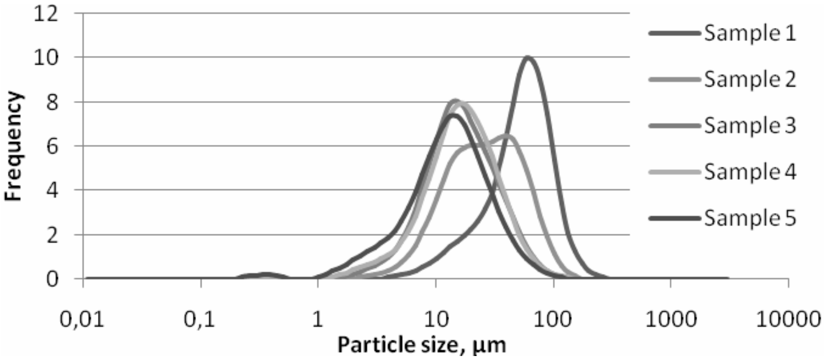

*Figure 3. The particle size distribution of the ground samples*

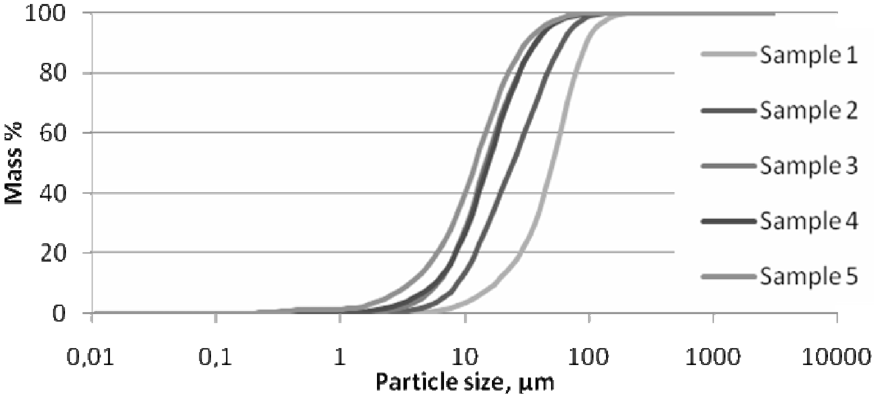

*Figure 4. The cumulative particle size distribution of the ground samples*

### 1.2. Heat treatment in furnace

Thermal behavior of gibbsite is known to display differences for natural and synthetic materials. An endothermic reaction at ~260 °C is characteristic for synthetic gibbsites [12]. One of our goals in our investigations was to observe the material which occurs during endothermic reaction. Thus, combined X-ray diffraction, heat treatment in furnace and thermal analytical experiments were performed.

The material was investigated in raw and ball-milled for 15 min (sample 5) states. All samples were spiked with zincite (ZnO) as internal standard (16.6wt%) and homogenized in an agate mortar, then heated in laboratory furnace (Nabertherm, with ±5 °C thermal inertia) at 260 °C for 30 minutes to simulate the reaction observed by DTA.

### 1.3. Measurements

TA measurements were performed on a MOM Derivatograph-C PC controlled thermal analysis system and Setaram Setsys 24 controlled by Setsoft 2000, by simultaneous thermogravimetry (TG), derivative thermogravimetry (DTG) and differential thermal analysis (DTA). A reference material of $\alpha$-$Al_2O_3$ was used, in similar volume as the measured samples. Evaluation of the results obtained by the MOM Derivatograph was done with the MOM Winder software. The base-line correction of DTA curves was done with measured correction data and polynomial smoothing was applied to remove static noise from the curves. The used heating rates were 10 K $min^{-1}$ [13–15].

XRD measurments were performed on a Bruker D8 Advance diffractometer equipped with a Cu-K$\alpha$ source (40kV, 40mA), a primary Göbel-mirror with 2.5° axial-Soller and 0.6mm exit slits and Grazing Incidence Soller with point detector. Data processing was carried out in Diffrac*Plus* EVA, data was prepared for Searh/Match by K$\alpha_2$-subtraction (Rachinger), Fourier-polynomial filtering and polynomial background subtraction. Search/Match was run on ICDD PDF2(2005). Quantification of results was made through Rietveld-refinement in TOPAS3, using FPA (Fundamental Parameters Approach) convolution for instrumental contribution. Crystal structure information was retrieved from Crystallography Open Database (COD), preferred orientation (PO) was corrected by the March-Dollase method. Powder specimens were prepared in agate mortar by manual grinding to avoid dehydration.

## 2. Experimental results and discussion

### 2.1. TG-DTA

The thermal decomposition of the aluminum hydroxides takes place in more steps. All of them are endothermic reactions. The first step is the gibbsite-boehmite transformation in the temperature range of 220–270 °C. The next step is the decomposition of residual gibbsite into oxides between 270 and 390 °C. The third step is the decomposition of boehmite above 480 °C. The final TG weight loss taken from 220 °C to 1000 °C is 34.4%, which corresponds to the stoichiometric values.

The TG-DTG and DTA curves of the unground and ground and not heat treated samples are shown at the 0 and 6. It is visible, that grinding decreased the magnitude of the decomposition pathway via boehmite. The loss of mass above the temperature 450 °C decreases increasing the grinding time: the mass loss of the unground sample above 450 °C is 5.88%, while in case of Sample 5 it is 4.40%. The corresponding molar ratio changes are 0.35 and 0.26 respectively.

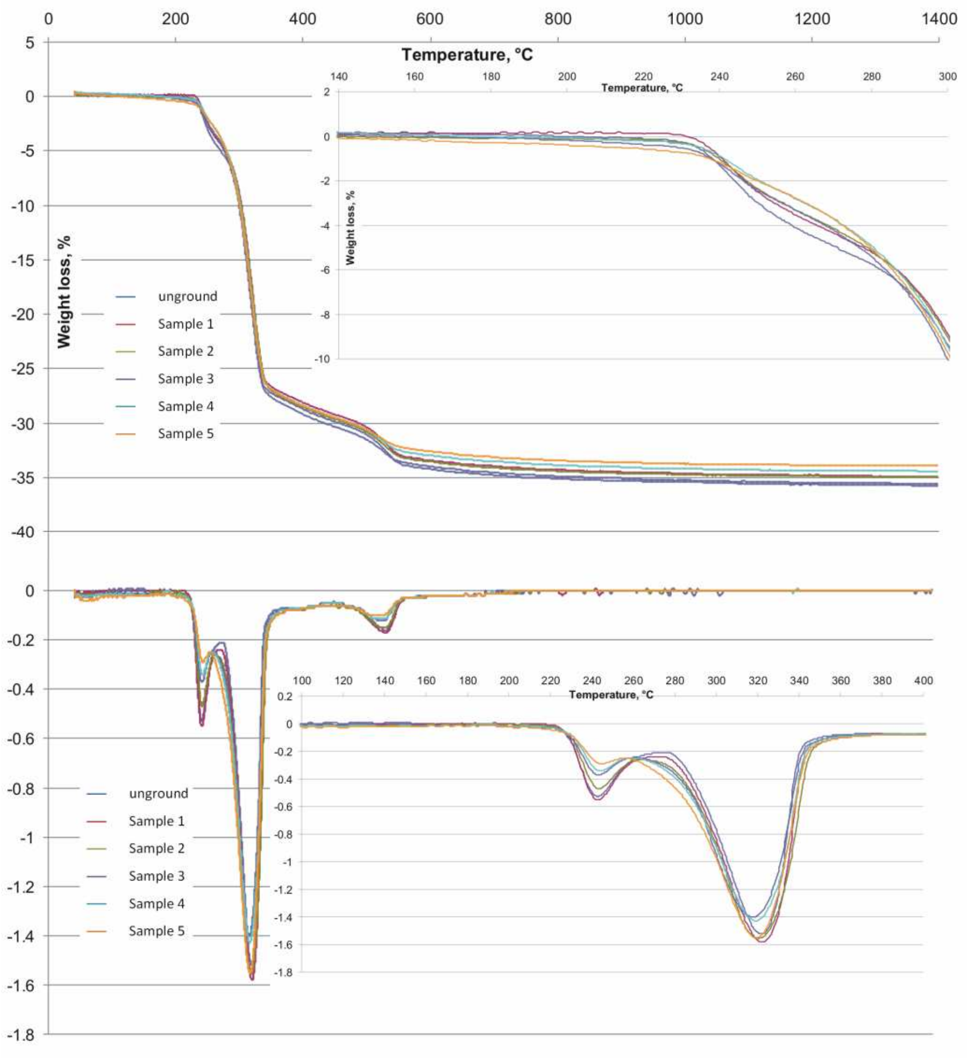

*Figure 5. TG and DTG curves of the unground or ground and previously not heat treated aluminum hydroxide samples, in the function of temperature.*
*Above: TG, %; below: DTG, mg/min*

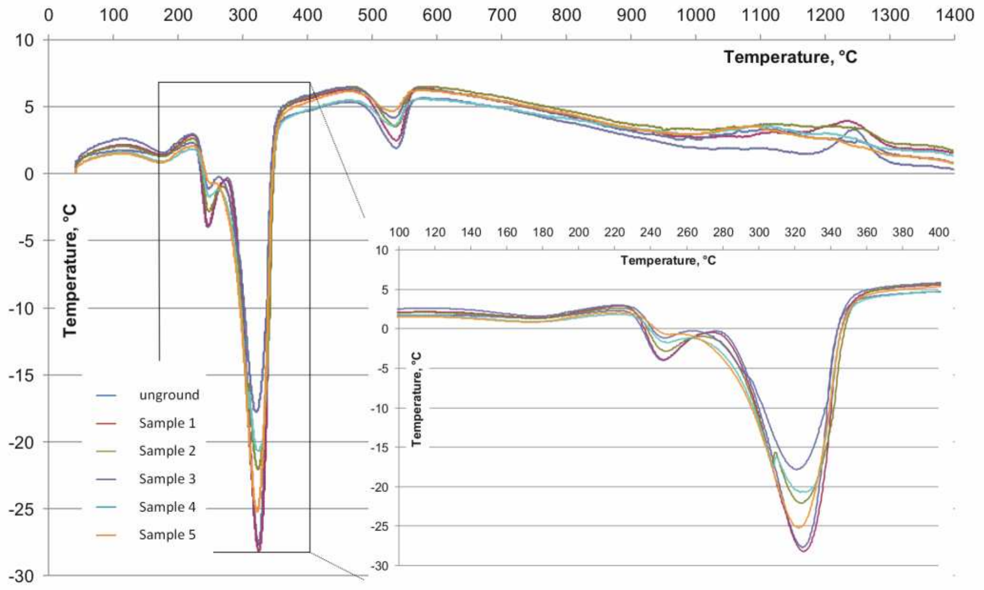

*Figure 6. DTA curves of the unground or ground and previously not heat treated aluminum hydroxide samples, heat effects in the function of temperature*

The heat treatment at 260 °C was carried out on the unground and 15 min ground (Sample 5) samples. The thermal curves of the heat treated samples are shown on the 0. The presence of boehmite formed by the heat treatment is more accentuated in the unground sample. In spite the fact that heat treatment was carried out at 260 °C, the weight loss begins below 100 °C. The possible explanations are given in the following sections.

### *2.2. X-Ray powder diffraction*

Rietveld-refinement on unheated and heated samples enabled us to determine the amorphous content by the internal standard method. However, PO severely affected the refinement in the non milled sample, due to the sub-micrometric platy crystallites. Both samples were found to contain some amorphous material, although TG showed that weight loss almost equals the $H_2O$ content of the 100% crystalline gibbsite material (Table 2). The results show that grinding increased the amorphous content of the sample, whereas the boehmite content after heat treatment is almost three times reduced in the ground material compared to the unground.

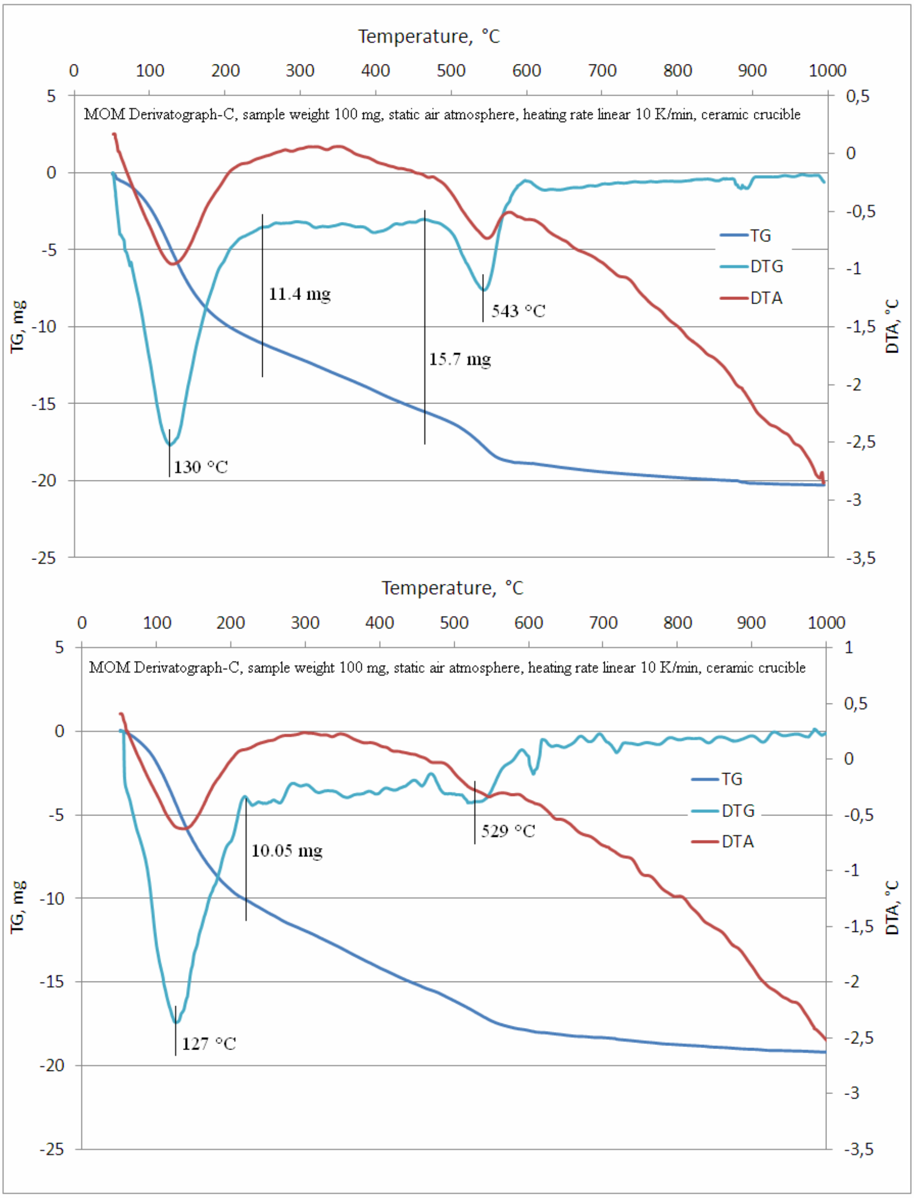

*Figure 7. TG, DTG, DTA curves of the heat treated aluminum hydroxide samples, heat effects and mass loss in the function of temperature, above: unground sample, below:15 min ground sample*

*Table 2*

*The composition (Rietveld-refinement, XRD)*
*of the samples heated and unheated*

| | **Unheated** | | **Heated at 260 °C** | |
|---|---|---|---|---|
| Phases | **Unground** | **Ground for 15 min** | **Unground** | **Ground for 15 min** |
| Gibbsite | 89,646 | 74,817 | | |
| Boehmite | | | 15,282 | 6,636 |
| Amorphous | 10,354 | 25,183 | 84,718 | 93,364 |

The role of heating was to observe whether intermediate hydrous compounds develop during this reaction or direct boehmite formation is going on. Weight losses of ~13% for ground aluminum hydroxide and ~16% for the unground sample were recorded. The second XRD investigation revealed that gibbsite has decomposed from both samples and boehmite together with an undetermined compound has formed. The undetermined compound is observed as one single broad peak, resembling the gibbsite (*002*) shifted to lower d(Å) value. This could indicate that a gibbsite pseudo-hydrate has formed, but without detailed spectroscopic and crystallographic characterization it is not possible to conclude on its nature. In Rietveld-refinement this undetermined product was considered as part of the amorphous content (Figure 8 and 9).

However, TA analysis performed on material dehydrated at 260 °C taken in a few days revealed that rehydration occurred, since the endothermic peak associated with weight loss starting at the beginning of the analysis cannot be interpreted by other processes. XRD taken on heated materials after several days did not evidence any gibbsite or newly crystallized hydrated compound. Thus, the phenomenon is explained by $H_2O$ shell formation around crystalline AlOH and amorphous AlOH or $Al_2O_3$.

To find out what is the approximate composition of the amorphous component(s) quantified by Rietveld-refinement, TA and heating in furnace was completed also with the drying experiment. Samples of unground and milled aluminum hydroxides were long-term dried at 60 °C. After 3 hours, a weight loss of 3.2% for milled and 1.8% for unground material was registered, and these values were preserved during the 3 days drying at constant temperature.

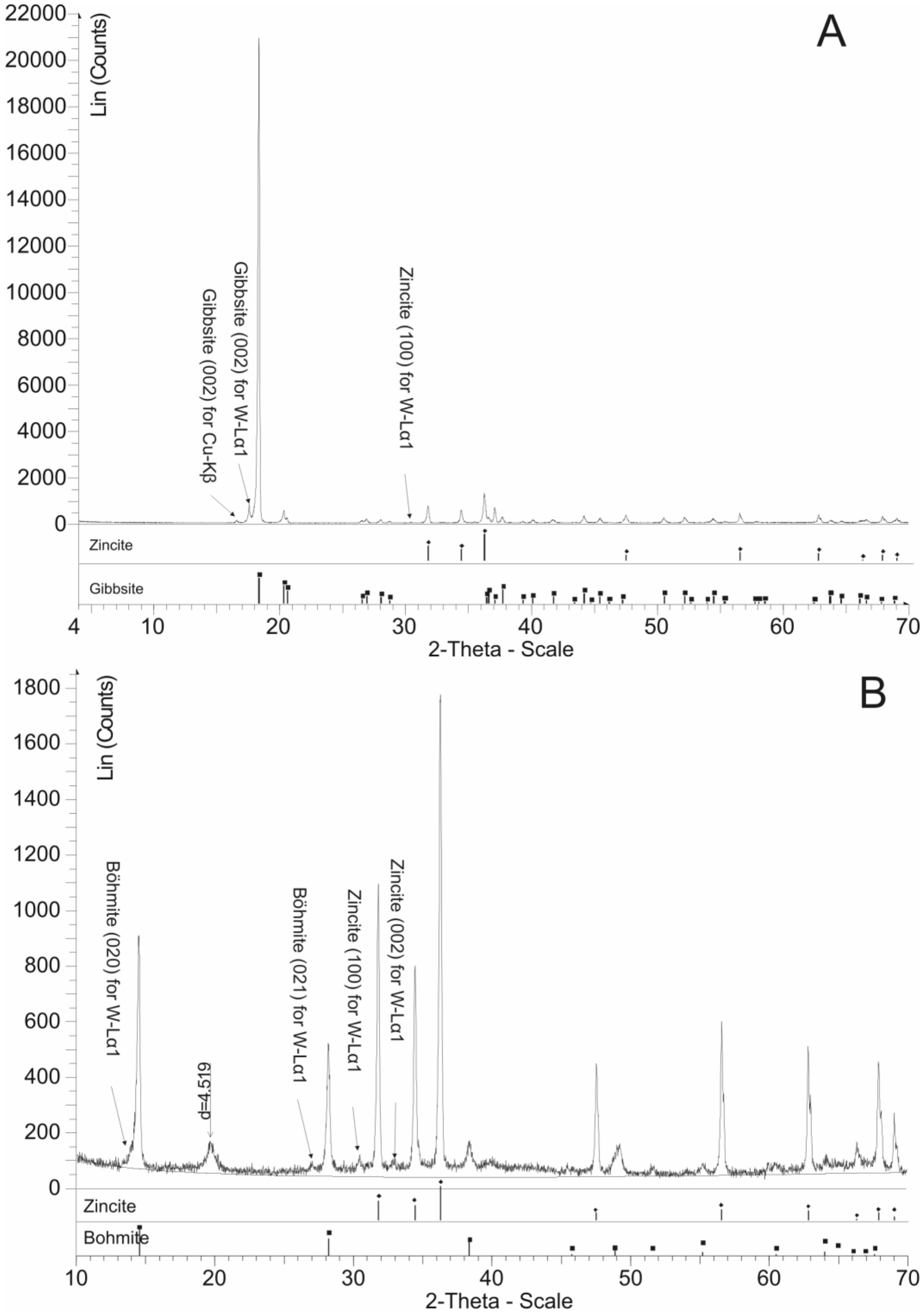

*Figure 8. XRD patterns of the unground samples; A: unheated; B: heated*

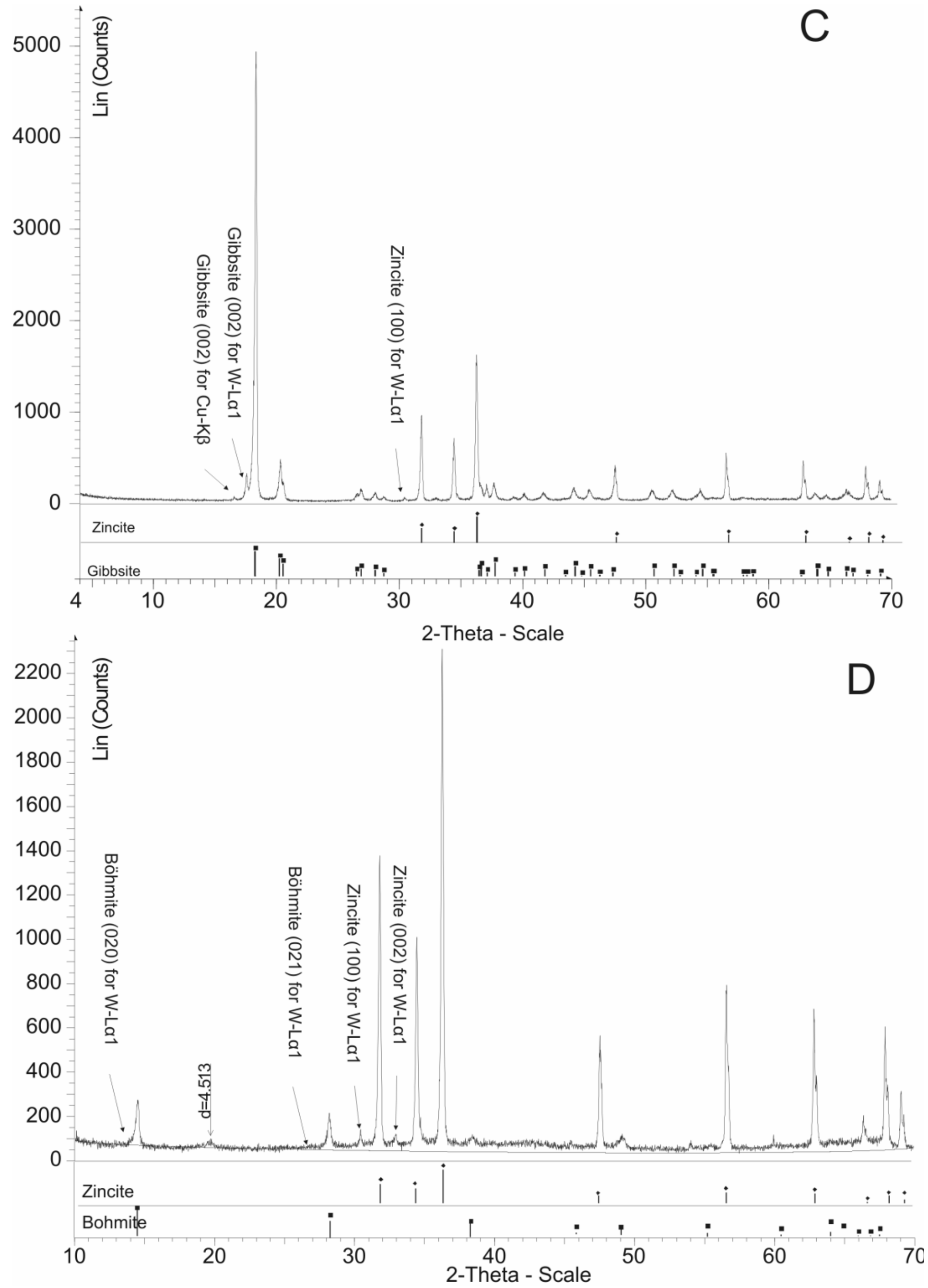

*Figure 9. XRD patterns of the ground samples; C: unheated; D: heated*

## Conclusions

Summarizing our results, we conclude that the original aluminum-hydroxide material contains at least two types of amorphous materials: $H_2O$ as fluid inclusion in gibbsite crystals and amorphous Al-compound with superficially bound $H_2O$.

The Rietveld-refinement for unground material indicated ~10% amorphous content, while the dehydration based on TG indicated 95% gibbsite. By drying experiment, $H_2O$ content of ~2% was found to be evaporated <80 °C where TA is unreliable.

The grinding of the material increased the amorphous content of the aluminum hydroxide, whereas the significance of the thermal conversion pathway via boehmite decreased.

### Acknowledgments

*The work described was carried out as part of the TÁMOP-4.2.1.B-10/2/KONV-2010-0001 project in the framework of the New Hungarian Development Plan.*

### References

[1] Gitzen, Walter H.: *Alumina as a Ceramic Material*. Westerville: The American Ceramic Society

[2] Mercury, H. M. R. et al.: *On the Decomposition of Synthetic Gibbsite Studied by Neutron Thermodiffractometry*. 2006., Journal of the American Ceramic Society, pp. 3728–3733.

[3] Perander, Linus Michael.: *Evolution of Nano- and Microstructure During the Calcination of Bayer Gibbsite to Produce Alumina*. Auckland: The University of Auckland, 2010. PhD dolgozat.

[4] Gan, Bee K, Madsenb, Ian C.–Hockridge, James G.: *In situ X-ray diffraction of the transformation of gibbsite to a-alumina through calcination: effect of particle size and heating rate.* Journal of Applied Crystallography: ismeretlen szerző, 2009., 42. kötet, pp. 697–705.

[5] Rouquerol, J.–Ganteaume, M.: *Thermolysis under vacuum: Essential influence of the residual pressure on thermoanalytical curves and the reaction products*. 1977., Journal of Thermal Analysis, pp. 201–210.

[6] Wittmann, Zs. et al.: *Phase Composition Analysis of Hydrous Aluminium Oxides by Thermal Analysis and Infrared Spectrometry*. 1992., Talanta, pp. 1583–1586.

[7] MacKenzie, K. J. D.–Temuujin, J.–Okada, K.: *Thermal decomposition of mechanically activated gibbsite.* 1999., Thermochimica Acta, pp. 103–108.

[8] Koga, N.: *A comparative study of the effects of decomposition rate control and mechanical grinding on the thermal decomposition of aluminum hydroxide.* 2005., Journal of Thermal Analysis and Calorimetry, pp. 595–601.

[9] Koga, N.–Fukagawa, T.–Tanaka, H.: *Preparation and Thermal Decomposition of Synthetic Bayerite.* 2001., Journal of Thermal Analysis and Calorimetry, pp. 965–972.

[10] Genc, Gözde.: *Processing and Characterization of Nanocrystalline Materials.* Izmir,Turkey: Izmir Institute of Technology, 2004.

[11] Jadambaa, Temuujin: *Mechanochemical Treatment of Solid Mixtures – a Promising Way of Synthesizing Ceramic Precursors*. Химия в интересах устойчивого развития, 2001., pp. 589–595.

[12] Földvári, M.: *Handbook of thermogravimetric system of minerals and its use in geological practice*. Budapest, Magyar Állami Földtani Intézet, 2011.

[13] Arnold, M. et al.: *The Derivatograph-PC – A New Type of Personal Computer-controlled Derivatograph*. 1990., Journal of Thermal Analysis, pp. 2693–2699.

[14] Arnold, M. et al.: *The Derivatograph-C – A Microcomputer-controlled Simultaneous TG, DTG, DTA, TD and EGA Apparatus. Part II. A Simple Method of Estimating Parameters.* 1987., Journal of Thermal Analysis, pp. 679–683.

[15] Gruin, I.–Sas, A.: *Application of the Q-Derivatograph for Evaluation of the Melting Enthalpies of Low-melting Compounds*. 1985., Journal of Thermal Analysis, pp. 803–811.

*Materials Science and Engineering, Volume 38/1. (2013), pp. 29–39.*

# PURIFICATION OF WASTEWATERS CONTAINING ENDOCRINE DISRUPTING COMPOUNDS BY COAGULATION

RENÁTA MÉSZÁROS[1]–SÁNDOR BÁRÁNY[1]

The paper represents a review of literature data on treatment of wastewaters containing endocrine disrupting compounds (EDC), first of all estrogenic hormones, which have been detected in influents and effluents of sewage treatment plants (STP), surface and drinking waters in many countries. A short description of typical representatives of EDCs, their composition and sources of origin is given. The current data and results of EDC/PPCP (pharmaceutical and personal care products) removal during conventional water treatment in surface water treatment plants (SWTP) are summarized. Conventional SWTPs

typically treat water by coagulation using alum, ferric chloride, and/or synthetic polymers followed by flocculation, sedimentation, filtration, and disinfection. Alternative SWTP designs or modifications of conventional WTPs include additional water treatment processes, e.g., use of activated carbon, biofiltration, membranes, aeration, chemical softening, ultraviolet light irradiation. The efficiency of removal of EDCs and first of all of their most dangerous representatives bisphenol A and nonyl-phenol using coagulation by aluminium sulphate and polyaluminium chloride is considered in detail.

**Keywords:** endocrine disruptor; pharmaceutical; coagulation, water treatment; review.

## Introduction

For over 70 years, scientists have reported that certain synthetic and natural compounds could mimic natural hormones in the endocrine systems of animals. These substances are now collectively known as endocrine-disrupting compounds (EDCs), and have been linked to a variety of adverse effects in both humans and wildlife. More recently, pharmaceuticals and personal care products (PPCPs) have been discovered in various surface and ground waters, some of which have been linked to ecological impacts at trace concentrations. The majority of EDCs and PPCPs are more polar compounds, than traditional contaminants and several have acidic or basic functional groups. These properties, coupled with the occurrence at trace levels create unique challenges for both removal processes and analytical detection. Reports of EDCs and PPCPs in water have raised substantial concern among the public and regulatory agencies; however, very little is known about the fate of these compounds during drinking and wastewater treatment [1].

Estrogenic hormones have been detected in influents and effluents of sewage treatment plants (STP) in many countries [2], surface water [3], as well as drinking water [4]. Considering the widespread occurrence and potential impacts of EDCs, it is highly important to remove them before discharge. The current data suggest that wastewater treatment processes have variable performance in removing EDCs.

---

[1] University of Miskolc, Institute of Chemistry
3515 Miskolc-Egyetemváros, Hungary
akmbsab@uni-miskolc.hu
fkmmr@uni-miskolc.hu

It is generally accepted that the three major classes of endocrine disruption endpoints are estrogenic (compounds that mimic or block natural estrogen), androgenic (compounds that mimic or block natural testosterone), and thyroidal (compounds with direct or indirect impacts to the thyroid) [5]. The majority of research has focused on estrogenic compounds. The most frequently studied structures of EDCs can be seen on Figure 1.

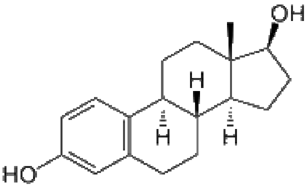

17β-Estradiol

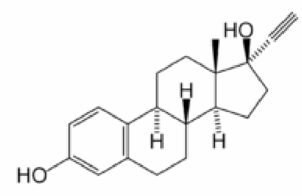

17α-Ethynyl Estradiol

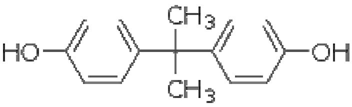

Bisphenol A (BPA)

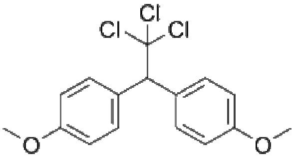

Methoxychlor

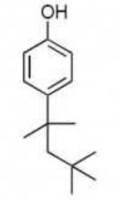

Octylphenol

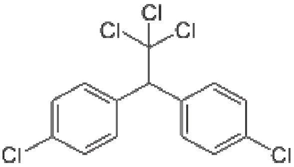

DDT

*Figure 1. Structures of the most frequently studied estrogenic compounds*

Endocrine disruption also can be caused by naturally occurring compounds. For example, estrogens from plant sources, known as phytoestrogens, have been linked to reproductive failures in animals since the 1930s [6].

Some scientists have suggested that some drinking water disinfection byproducts may act as EDCs.

Many of the thousands of anthropogenic chemicals currently released into the environment are endocrine-disrupting compounds (EDCs); a typical representative of them is bisphenol-A (see Figure 1). It has become one of the most dangerous pollutant in the environment within the past 80 years because of its presence in a multitude of products including food and beverage packaging, flame retardants, adhesives, building materials, electronic components, and paper coatings [7].

There are a number of papers as well as reviews devoted to problem of purification of drinking and industrial wastewaters from endocrine disrupting compounds. The most efficient methods are adsorption on activated carbon and oxidation by ozone and chlorine [8]. At the same time coagulation by multivalent salts hydrolysis products and/or adsorption on freshly precipitated hydrolysis products particles could serve as an alternative or additional method of EDCs removal taking into account that coagulation is an obligatory stage of water conditioning in the majority of waterworks. Combination of coagulation with adsorption can give good results in the process of treatment of waters containing EDCs and PPCPs. Our paper gives a review of updated results in this area.

## 1. EDC/PPCP removal during conventional water treatment

Some of the most representative PPCPs found in Sewage Treatment Plants (STP) are antibiotics, lipid regulators, anti-inflammatory agents, tranquillizers, contrast media and contraceptives with very different chemical structures.

Most of these compounds come either from domestic sewage or from hospital as well as industrial discharges and enter municipal STPs. Modern STPs can effectively accomplish carbon and nitrogen removal, as well as microbial pollution control [9].

Recent studies have shown that the elimination of PPCPs in municipal STPs is often incomplete [10], with efficiencies ranging between 60% and 90% for a variety of polar compounds. Their removal can be attributed not only to biodegradation, but also to adsorption onto solid surfaces [11, 12]. As a consequence, significant fractions of PPCPs are discharged with the final effluent of the STP into the aquatic environment. A major factor influencing the efficiency of pollutants removal from water is their ability to interact with solid particles, both natural (clay, sediments, microorganisms) and added to the medium (active carbon, coagulants), because this facilitates their removal by physical-chemical (settling, flotation) or biological processes (biodegradation). However, compounds with low adsorption coefficients tend to remain in the aqueous phase, which favors their mobility through the STP and the receiving environment [13]. In this way, many PPCPs remain in the aqueous phase, such as the anti-inflammatories and the antibiotics, whereas some of them are adsorbed to the sludge, such as the estrogens [14].

The overall removal rates published in literature vary strongly. In Germany, the reported efficiencies range from 10% to 90% depending on the nature of the compound [10]. In Brazil, the removal efficiencies for pharmaceutical polar compounds vary from 12% to 90%, where the efficiencies obtained in activated sludge processes were higher than those of obtained in biofilters [15]. Another study, carried out in the USA concluded that many PPCPs (around 80%) were removed [16]. In all these cases, the removal includes both degradation and adsorption and the difference between the two mechanisms has not been assessed yet. In the case of polar compounds, such as carboxylic acids, for which the adsorption effects are expected to be very low, the main mechanism of elimination is attributed to biodegradation.

Conventional surface water treatment plants (SWTPs) typically treat water via coagulation using alum, ferric chloride, and/or synthetic polymers followed by flocculation, sedimentation, filtration, and disinfection. Conventional SWTPs achieve high removals of pathogens and other biological particles, and modest removal of dissolved organic carbon (DOC, 1 to 10 mg/L). In the United States, chlorine and chloramines are typically used for disinfection, while ozonation is more commonly practiced in European countries. Alternative SWTP designs or modifications to conventional WTPs sometimes include additional water treatment processes (e.g., adsorption on activated carbon, biofiltration, membranes, aeration, chemical softening, and ultraviolet light irradiation).

By comparing the influent and effluent estrogen concentrations, authors [2] concluded that the removal efficiency for estrone (E1) and 17b-estradiol (E2) were 87 and 61%, respectively. In a study of 20 STP in Sweden, the average removal efficiency was 81% by activated sludge treatment and only 28% by solid supported bacterial treatment. Therefore it is essential to install additional treatment processes after the secondary treatment step, to ensure a more complete removal of such compounds.

The attenuation of PPCPs in receiving waters and in drinking water treatment plants also has been demonstrated in several studies and has been reviewed recently [17]. For example, the attenuation of several PPCPs was observed as secondary wastewater effluent was infiltrated into groundwater [18] and during river bank filtration [17]. In contrast to the efficient removal of many PPCPs observed in saturated and unsaturated groundwater, conventional drinking water treatment plants do not appear to remove PPCPs well. For example, clofibric acid has been detected at concentrations as high as 270 ng/L in drinking water from Berlin [19]. Of 47 wastewater tracers and EDCs analyzed, 15 were detected in raw drinking water (river water) samples, and 14 in finished drinking water samples from Atlanta [20].

## 2. Chemical precipitation processes

Metal salts (aluminum sulfate, ferric chloride) and softening chemicals (calcium oxide, sodium carbonate) are commonly added to destabilize particles present in water or to precipitate new particles (coagulation), aggregate particles (flocculation), and improve settling characteristics of particles (clarification). Sand filtration is commonly used after clarification for additional particle removal. Natural organic matter and EDCs or PPCPs may adsorb to particles in water and metal hydroxide particles formed during coagulation. Furthermore, chemical precipitation can remove moderately hydrophobic organic contaminants that have a strong affinity for adsorbed natural organic matter [1].

However, very little is known about the association of EDCs or PPCPs to particles present in water treatment systems. Therefore, it is difficult to make a priori predictions about the removal of EDCs or PPCPs during chemical precipitation processes.

An insight to the problem can be obtained by considering the behavior of pesticides, herbicides, and polycyclic aromatic hydrocarbons during chemical precipitation processes. Partitioning of organic compounds onto particles can occur through several mechanisms.

Some of the more hydrophobic compounds are present in wastewater effluents, but may not occur in raw drinking water supplies [20]. Some surfactants include both polar and non-polar moieties. The partitioning of octylphenol in English river sediments was the highest to the clay and silt fraction of the sediments, suggesting a hydrophobic interaction with organic carbon as well as surface area associated with the clay and silt particles [21]. As a result, only a few compounds (e.g., bisphenol A, E2, 17-alpha ethinylestradiol, octylphenol, polycyclic aromatic hydrocarbons) could be associated with organic phases of particles in drinking water treatment plants.

In addition to hydrophobic partitioning, organic contaminants can be adsorbed to particles by interactions of polar functional groups with charged particles and mineral surfaces by complexation or ion exchange. For example, the observed sorption of many polar pharmaceuticals (e.g., tetracycline) to soil and sediment is considerably stronger than predicted by hydrophobic interactions alone [22]. Such interactions could be particularly important in drinking water treatment, where mineral oxides provide a relatively high density of surface functional groups that could interact with polar pharmaceuticals. For example, approximately 25% of the nonylphenols in groundwater were removed during coagulation with alum [23]. Therefore, it is possible that some polar EDCs or PPCPs could be removed during coagulation.

Despite the predictions, available data from pilot and full-scale water treatment plants indicate that removal will be modest at best. Neither lime softening nor alum coagulation (conventional or enhanced dosages ranging from 6 to 18 mg/L) demonstrated atrazine removal. Coagulation/flocculation/sedimentation with alum and iron salts or excess lime/soda ash softening did not result in significant removal of antibiotics (i.e. sulfachlorpyridazine, sulfadimethoxine, sulfamerazine, sulfamethazine, sulfathiazole, and trimethoprim). In another study, ferric chloride precipitation did not remove several pharmaceuticals frequently detected in surface waters (diclofenac, carbamazepine, bezafibrate). Certain pesticides were poorly removed by coagulation and 50% of the pyrene, fluoranthene, and anthracene were removed through hydrophobic interactions. On the basis of predictions of hydrophobic interactions and results of full-scale measurements, it was concluded that EDCs and PPCPs not associated with colloidal or particulate material will most likely be poorly removed during coagulation [1].

Park [24] studied the effects of aluminum chloride on activated sludge performance and removal of 17-alpha ethinylestradiol, four 10 L activated sludge reactors that only varied in influent aluminum concentrations were operated. Aluminum was added in 0.1, 0.5, 1.5, and 2.5 mg/L concentration to the influent wastewater.

The laboratory reactor study has shown that aluminium in influent wastewater exhibits significant positive impact on the bioflocculation of activated sludge. A correlation between effluent suspended solids, particulate-colloidal biopolymers, and 17-alpha ethinylestradiol concentrations were established. The following conclusions are drawn from this study:

- Higher Al-fed activated sludge led to better biomass settling and dewatering properties.
- Higher Al-fed systems resulted in lower effluent, total suspended solids (TSS) and lower particulate-colloidal biopolymers in the effluent.
- Higher Al-fed activated sludge resulted in better removal of 17-alpha ethinylestradiol.
- Alum plays very important role in activated sludge bioflocculation and it also enhances the removal of EDCs in wastewater treatment systems [24].

Xiaoying discussed [25] the coagulation characteristics of bisphenol-A with polyaluminum chloride (PACl-$Al_{13}$) as coagulant, examined the impact of coagulation pH, PACl-$Al_{13}$ dosage, total organic carbon and turbidity on bisphenol-A removal, and analyzed the possible dominant mechanisms in water coagulation process.

Formation and performance of flocs during coagulation processes were monitored using photometric dispersion analyzer. When the concentration of humic acid matters and turbidity was low in the solution, the experimental results showed that the removal of bisphenol-A increases and subsequently decreases with the PACl-$Al_{13}$ dosage increasing. The optimal PACl-$Al_{13}$ dosage was found at bisphenol-A/PACl-$Al_{13}$ = 1:2.6(M/M) in the experimental conditions. Results show that the maximum bisphenol-A removal efficiency occurred at pH 9.0 due to the adsorption of bisphenol-A onto $Al_{13}$ aggregates rather than the charge neutralization mechanism by polynuclear aluminous salts in the solution. The humic acid matters and kaolin in the solution have significant effect on bisphenol-A removal with PACl-$Al_{13}$ in the coagulation. The bisphenol-A removal will be weakened at high contents of humic matters. The removal rate of bisphenol-A increased and subsequently decreased with the turbidity increasing.

To characterize the relationship between coagulant dosage and settling performance (turbidity/TOC removal) the floc formation rates were measured using PDA. The content of bisphenol-A in the tested water was 5.0 mg/L. The effect of coagulant dosage on the bisphenol-A removal was examined at 5, 7, 9, 10, 11, 13, 15, 17.5 and 3.37 mg/L of total organic carbon, and pH 7.0 [25].

As shown in Figure 2, an increase in PACl-$Al_{13}$ dose from 1 to 13 mg/L, improved the bisphenol-A removal in the settling process. The maximum bisphenol-A removal efficiency was 26.8%, and it was reached at zeta potential close to the isoelectric point of hydrolysis product particles. The results indicate that the dominant removal mechanism at pH 7.0 is the charge neutralization of large negatively charged natural colloids by positively charged hydrolysis product particles of hydrolyzing salts. This promotes agglomeration of destabilized colloids [25]. The mechanisms of interaction of aluminium salts hydrolysis product particles with different contaminants and efficiency of water treatment by hydrolysing salts are discussed in detail in our review [30].

At higher PACl-$Al_{13}$ dosage, the interaction between voluminous aluminium hydroxide precipitates and natural colloids is known as sweep coagulation. The particles are destabilized by adsorption on aluminium hydroxide sols and are enmeshed in sol aggregates, promoting the formation of relatively large, quickly sedimenting flocs. Thus, Bisphenol-A, which is not adsorbed initially, can be removed by enmeshment in the flocs [25].

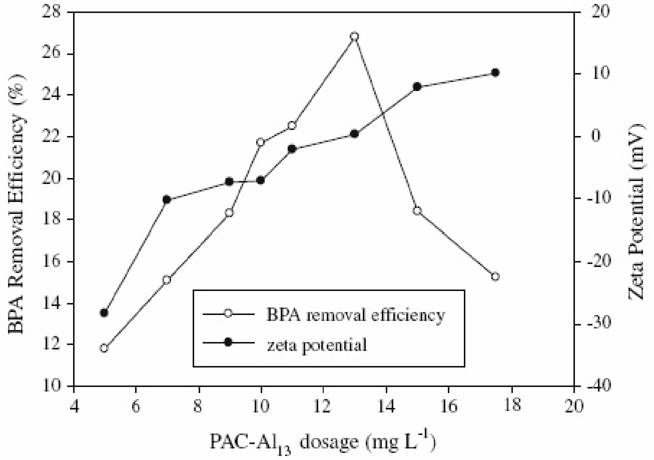

*Figure 2. Effect of PAC-$Al_{13}$ dosage on BPA removal efficiency and zeta-potential of 5 mg/L BPA solution (TOC = 3,36 mg/L, pH = 7) [25]*

Amirtharaja and Tambo [26] reported that the zeta potential of properly destabilized particles usually ranges between –4 mV to +3 mV. For these reasons it can be supposed that the optimum PACl-$Al_{13}$ dosage will correspond to that at which zeta potential of particles will be approximately zero. As shown in Figure 2, the bisphenol-A removal increased with the increase of coagulant dosages before reaching the optimal dosage, which was found at bisphenol-A/PACl-$Al_{13}$ = 1:2.6(M/M) In these conditions zeta potential remained negative but gradually approached zero. When zeta potential was reversed, the bisphenol-A removal decreased due to the re-stabilization of particles [25].

It has been shown that the flocs size vs. time increased as the PACl-$Al_{13}$ dosage increased from 5 to 13 mg/L (Figure 3). Higher dosage did not significantly increase the rate of floc formation. The floc growth follows the classical pattern composed of a short induction period followed by a rapid growth phase until the steady state floc size is reached. These data correlate with the results presented in Figure 2, which indicates that the mechanism might be re-stabilization of colloidal particles when over dose of coagulant was added [25].

## 3. Removal of low level contaminants by coagulation

Paper [27] describes the removal efficiency of bisphenol A and nonylphenol present in waters at low level, by conventional water treatment methods – coagulation/flocculation/ sedimentation, oxidation-chlorination and ozonation and adsorption on powdered activated carbon (PAC) and granular activated carbon. Coagulants tested were alum, poly-aluminum hydroxychloride (PACl), poly-aluminum silicate sulfate (PASS), poly-aluminum chloride silicate (PACS), and $Fe_2(SO_4)_3$. Results are presented in Table 1.

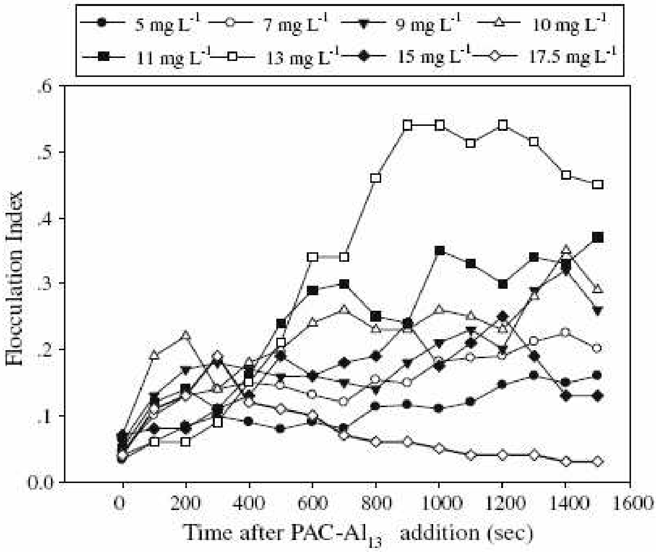

*Figure 3. Flocculation index vs time for eight PAC-$Al_{13}$ dosages [25]*

*Table 1*

*Removal of bisphenol-A and nonylphenol by coagulation, flocculation and sedimentation [27]*

| **Chemical** | **Initial conc.** | **alum 50** (mg/L) | **PACl 45** (mg/L) | **PASS 45** (mg/L) | **PACS 30** (mg/L) | $Fe_2(SO_4)_3$ 45 (mg/L) |
|---|---|---|---|---|---|---|
| **Bisphenol-A (μg/L)** | 1 | 0.93 | 0.96 | 0.94 | 0.96 | 0.94 |
| **Turbidity (NTU)** | 5.1 | 0.76 | 0.64 | 0.74 | 0.6 | 0.69 |
| **DOC (mg/L)** | 2.16 | 1.53 | 1.64 | 1.59 | 1.62 | 1.67 |
| **Nonylphenol (μg/L)** | 4.5 | 4.56 | 4.35 | 4.43 | 4.5 | 4.4 |
| **Turbidity (NTU)** | 9.4 | 0.82 | 0.7 | 0.76 | 0.63 | 0.77 |
| **DOC (mg/L)** | 2.25 | 1.62 | 1.5 | 1.58 | 1.6 | 1.57 |

It can be seen that the turbidity index dropped from 5.1–9.4 to 0.60–0.82 nephelometric turbidity units (NTU) and dissolved organic carbon (DOC) concentrations decreased from 2.16–2.25 to 1.5–1.67 mg/L. Despite the fact that DOC decreased by 26–30%, removal efficiencies of nonylphenol and bisphenol were only 4–7% and 0–3%, respectively.

Spiked EDCs did not appear to be adsorbed onto natural organic matter completely during 30 minutes of coagulation/flocculation/sedimentation. The type of coagulant used did not affect the EDC removal efficiency significantly. Chemical precipitation using iron and aluminum salts was found to be ineffective in removing estrogen [28] and pharmaceuticals [29].

## Conclusions

1. Endocrine disrupting compounds (EDC) have been detected in influents and effluents of sewage treatment plants (STP), surface and drinking waters in many countries.
2. The most efficient methods of removal of EDCs from waters are adsorption on activated carbon and oxidation by ozone and chlorine. At the same time coagulation by multivalent salts hydrolysis products and/or adsorption on freshly precipitated hydrolysis products particles could serve as an alternative or additional method of EDCs removal taking into account that coagulation is an obligatory stage of water conditioning in the majority of waterworks. Combination of coagulation with adsorption can give good results in the process of treatment of waters containing these contaminants.
3. Elimination of Pharmaceutical and Personal care products (PPCPs) in municipal Sewage Treatment Plants (STPs) can reach 60%–90% depending on the polarity of the compounds to be removed. Their removal can be attributed to biodegradation, and also to adsorption onto solid surfaces.
4. The removal efficiency of bisphenol A and nonylphenol, as the most dangerous representatives of EDCs, by coagulation using aluminum sulphate and poly-aluminum chlorides has been studied in a number of works. The conventional

coagulation/flocculation water treatment process had very low removal efficiencies for bisphenol A (0–3%) and nonylphenol (4–7%).

5. The degree of EDCs removal from waters with relatively high contents of pollutant in the presence of big doses of poly-aluminum-chlorides can reach 26–28%. The mechanism of removal is "sweep" coagulation, i.e. entrapment of contaminants between the freshly precipitating hydrolysis product particles [$Al(OH)_3$], i.e. by their enmeshment in the forming flocs.

## Acknowledgements

*The described work was carried out as part of the TÁMOP-4.2.1.B-10/2/KONV-2010-0001 project in the framework of the New Hungarian Development Plan. The realization of this project is supported by the European Union, co-financed by the European Social Fund.*

## References

[1] Snyder, S. A.–Westershoff, P.–Yoon, Y.–Sedlak, D. L.: *Pharmaceuticals, Person Care Products, and Endocrine Disruptors in Water: Implycations for the Water Industry.* Env. Eng. Sci., 2003, 20, 449.

[2] Baronti, C.–Curini, R.–D'Ascenzo, G.–Di Corcia, A.–Gentili, A.–Samperi, R.: *Monitoring natural and synthetic estrogens at activated sludge sewage treatment plants and in a receiving river water*. Environ Sci technol., 2000, 35, 5059.

[3] Liu, R.–Wilding, A.–Zhou, J.: *Microwave-assisted extraction followed by gas chromatography-mass spectrometry for the determination of endocrine disrupting chemicals in river sediments*. Chromatogr., 2004, 1022, 179.

[4] Kuch, H. M.–Ballschmiter, K.: *Determination of endocrine-disrupting phenolic compounds and estrogens in surface and drinking water by HRGC−(NCI)−MS in the picogram per liter range.* Environ Sci Tenchnol, 2001, 35, 3201.

[5] EPA. (1997) *Special report on environmental endocrine disruption: An effects assessment and analysis*. Washington, DC: Office of Research and Development. EPA/630/R 96/012.

[6] Walker, B. S.–Jenney, J. C.: *Estrogenic substances. II. Analysis of plant sources.* Endocrinology, 1930, 14, 389.

[7] Staples, C. A.–Dorn, P. B.–Klecka, G. M.–O'Block,S. T.–Harris, L. R.: *A review on the environmental fate, effects, and exposures of bisphenol A.* Chemosphere, 1998, 36, 2149.

[8] Mészáros, R.: *Élőlények hormonrendszerét befolyásoló anyagok eltávolítása hagyományos vízkezelési eljárásokkal*. Magyar Kémikusok Lapja, 2012, 67, 268.

[9] Carballaa, M.–Omila, F.o–Lemaa, J. M.–Llompartb, M.–Jaresb, C. G.–Rodriguezb, I.–Go´mezc, M. T.: *Ternes Behavior of pharmaceuticals, cosmetics andhormones in a sewage treatment plant*. Water Research, 2004, 38, 2918.

[10] Ternes, T. A.: *Occurrence of drugs in German sewage treatment plants andrivers.* Water Res, 1998, 32, 3245.

[11] Stumpf, M.–Ternes, T. A.–Haberer, K.–Seel, P.–Baumann, W.: *Determination of drugs in sewage treatment plants andiver water*. Vom Wasser, 1996, 86, 291.

[12] Hirsch, R.–Ternes, T. A.–Haberer, K.–Kratz, K. L.: *Determination of betablockers and b-sympathomimetics in the aquatic environment.* Vom Wasser, 1996, 87, 263.

[13] Ohlenbusch, G.–Kumke, M. U.–Frimmel, F. H.: *Sorption of phenols to dissolved organic matter investigated by solid phase microextraction*. Sci Total Environ, 2000, 253, 63.

[14] Jensen, R. L.–Schafer, A. I.: *Adsorption of estrone and 17b bestradiol by particulates – activated sludge, bentonite, hematite andellulose*. Recent Advances in Water Recycling Technologies Workshop, Brisbane, 26 November 2001, 93–102.

[15] Ternes, T. A.–Kreckel, P.–Mueller, J.: *Behaviour and occurrence of estrogens in municipal sewage treatment plants* – II. Aerobic batch experiments with activated sludge. Sci Total Environ, 1999, 225, 91.

[16] US Environmental Protection Agency, 2003. Pharmaceuticals and Personal Care Products (PPCPs) as Environmental Pollutants: Pollution from Personal Actions, Activities and Behaviors. Available in Internet in:
http://www.epa.gov/nerlesd1/chemistry/pharma>.

[17] Heberer, T.: *Occurrence, fate, and removal of pharmaceutical residues in the aquatic environment: A review of recent research data*. Toxicol. Lett, 2002, 131, 5.

[18] Drewes, J.–Heberer, T.–Reddersen, K.: *Removal of pharmaceuticals during conventional wastewater treatment, advanced membrane treatment and soil–aquifer treatment.* 2nd International Conference on Pharmaceuticals and Endocrine Disrupting Chemicals in Water, Minneapolis, MN. 2001.

[19] Heberer, T.–Dumnbier, U.: *Polar DDT metabolites as contaminants of surface, ground and drinking water in Berlin*. Nat. Groundwater Assoc. – Emer. Issues Conf., Minneapolis, 2000.

[20] Henderson, A. K.–Moll, D. M.–Frick, E. A.–Zaugg, S. D.: *Presence of wastewater tracers and endocrine disrupting chemicals in treated wastewater effluent and in municipal drinking water.* Nat. Groundwater Assoc., Atlanta, GA. 2001.

[21] Johnson, A. C.–White, C.–Besien, T. J.–Jurgens, M. D.: *The sorption potential of octylphenol, a xenobiotic oestrogen, to suspended and bed-sediments collected from industrial and rural reaches on three English rivers.* Sci. Total Environ, 1998, 210, 271.

[22] Tolls, J.: *Sorption of veterinary pharmaceuticals in soils*. Environ. Sci. Technol., 2001, 35, 3397.

[23] Fielding, M.–Harding, L.–James, C.–Mole, N.: *Removal of nonylphenol ethoxylates by water treatment processes*. UK WIR Report, 1998, 98/TX/01/5.

[24] Park, C.–Fang, Y.–Sudhir, N.–Murthy, C.–John, T.–Novak, D.: *Effects of floc aluminum on activated sludge characteristics and removal of 17-a-ethinylestradiol in wastewater systems*. Water Research, 2010, 44, 1335.

[25] Xiaoying, M.–Zeng, G.–Zhang, C.–Wang, Z.–Yu, J.–Li, J.–Huang, G.–Liu, H.: *Characteristics of BPA removal from water by PACl-Al13 in coagulation process.* Journal of Colloid and Interface Science, 2009, 337, 408.

[26] Amirtharaja, A.–Tambo, N. in: Amirtharajah, A.–Clark, M. M.–Trussell, R. R. (Eds.): *Mixing in Coagulation and Flocculation*. American Water Works Association Research Foundation, Denver, 1991, Chapter 1.

[27] Keun, J. C.–Sang, G. K.–Chang, W. K.–Jae, P. K.: *Removal efficiencies of endocrine disrupting chemicals by coagulation/flocculation, ozonation, powdered/granular activated carbon adsorption, and chlorination.* Korean J. Chem Eng., 2006, 23, 399.

[28] Svenson, A.–Allard, A. S.–Ek, M.: *Removal of estrogenicity in Swedish municipal sewage treatment plants.* Water Res., 2003, 37, 4433.

[29] Ternes, T. A.–Meisenheimer, M.–McDowell, D.–Sacher, F.–Brauch, H. J.–Haist-Gulde, B.–Preuss, G.–Wilme, U.–Zulei-Seibert, N.: *Removal of pharmaceuticals during drinking water treatment.* Environ. Sci. & Tech., 2002, 36, 3855.

[30] S. Bárány, S.–Mészáros, R.: *Alumínium sók hidrolízis termékeinek nanorészecskéi és alkalmazásuk a víztisztításban.* Magyar Kémiai Folyóirat, 2006, 112, 56.

*Materials Science and Engineering, Volume 38/1. (2013), pp. 41–50.*

# INVESTIGATION OF THE HYDRODYNAMIC PROPERTIES OF MAGNETICALLY STIRRED MOLTEN GALLIUM-INDIUM ALLOY BY NUMERICAL SIMULATION

CSABA NAGY[1]–LÁSZLÓ GYULAI[2]–
ARNOLD RÓNAFÖLDI[1]–ANDRÁS ROÓSZ[1]

An experimental crystallizer – equipped with magneto-hydrodynamic (MHD) stirrer – was built by the MTA-ME Materials Science Research Group, to investigate the factors influencing crystallization. Several quests were done to get information about the hydrodynamic behavior of the molten metal in the crystallizer during stirring. The experiments were done with Ga-In alloy, which is molten on room temperature. To get additional information, which is not possible to measure, a numerical model was made with ANSYS FLUENT numerical simulation program. The Lorentz-force field, which makes the Ga-In alloy rotate, was generated with a **U**ser **D**efined **F**unction (UDF) to completely reproduce the MHD stirrer's effects on the melt.

**Keywords:** numerical, simulation, gallium, indium, stirring, magnetic, magneto-hydrodynamic, MHD

## Introduction

Understanding crystallization in the industry is a very difficult task. In the case of continuous casting the ingot is not completely solid after it rolled out from the crystallizer. There are several complex flows inside, which have a strong effect on the structure and by this, on the mechanical, thermal, electrical, etc. properties. An experimental crystallizer – equipped with **magneto**-hydrodynamic stirrer – was built at the MTA-ME Materials Science Research group to understand these effects with controlled crystallizing. The magnetically stirred molten metal is lowered into water to be solidified. Several new structures can be made by this method. Because of the structure of the crystallizer, the hydrodynamic properties can't be examined well with classical methods. There were measurements on the free surface's sedimentation and the average angular velocity of the melt. These experiments were done with 74.5% Ga–25.5% In by A. Rónaföldi [1]. To get more information about what is happening in the melt a numerical model was made with ANSYS FLUENT 13.0. The induced Lorenz-force field – what's making the molten metal rotate – was made with a **U**ser **D**efined **F**unction (UDF). The work is discussed in the paper in details.

---

[1] University of Miskolc, Institute of Materials Science
3515 Miskolc-Egyetemváros, Hungary
ntsart@gmail.com
[2] University of Miskolc, Department of Combustion Technology and Thermal Energy
3515 Miskolc-Egyetemváros, Hungary

## 1. The MHD system

The mentioned crystallizer's stirrer works by the laws of Maxwell equations [1]. If the molten Ga-In alloy (**hereinafter** referred to as "gallium") is put into the rotating magnetic field, an eddy current will be induced in it. By the law of Lenz the melt will try to weaken the inducing effect, so it will start rotating (and making a potential vortex). Figure 1 shows a schematic setup of the system.

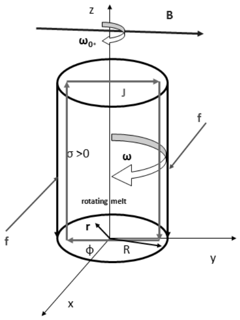

*Figure 1. The force system in the inductor*

The equation of the induced Lorenz force is:

$$f = \frac{1}{2}\sigma B^2 r(\omega_0 - \omega) \tag{1}$$

Where: $\sigma$ is the electric conductivity of the melt (S/m), $B$ is the magnetic induction (T), $r$ is the actual **radius** (m), $\omega_0$ is the synchronous angular velocity of the inductor (rad/sec), $\omega$ is the actual angular velocity of the melt (rad/sec).

By the effect of the force field the melt starts rotating and reaches a maximum angular velocity – an "equilibrium angular velocity". The melt can't reach the inductors synchronous angular velocity because of two main reasons. The first is visible in equation (1). As the melt accelerates, it stultifies the inducing force field. The second reason is the wall **friction**, which can extremely slow down the melts flow [2]. As can be seen on Figure 2, the melt's accelerating quickly first, but then reaches the maximum, which depends on the induction, the crucible's diameter etc.

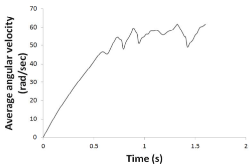

*Figure 2. Radial average angular velocity as a function of time – the settling of the flow*

## 2. Setup of the FLUENT model

The aim was to reproduce the gallium's flow with the measured parameters of A. Rónaföldi [1]. The data from the experiments with 10 mm, 25 mm and 35 mm diameter crucibles were chosen to be used in the FLUENT. The 10 mm is close to the crucible, which is used at the crystallization – with diameter of 8mm – the two other were used for checking the model's parameters.

Basically a 2D axisymmetric swirl solver was used with Volume of Fluid (VOF) multiphase model for 2 phases – the gallium and air. For the second, default material properties were used. The density of the melt was 6350 kg/m$^3$ and the viscosity was 0.00217 Pas. The turbulence was computed with a Realizable k-ε turbulence model (+ Enhanced Wall Treatment). Only the crucible was needed, so the simplified geometry was a simple rectangle – half cut of the cylindrical crucible's longitudinal slice – meshed with 45 000–75 000 hexa cells depending on the size of the crucible.

The Lorenz force field was programmed by a **U**ser **D**efined **F**unction (UDF). It's a C programming interface which contains eq. (1) with all of the time and coordinate dependent variables. These variables are the radius (***r***) and the gallium's current angular velocity (***ω***). The magnetic field has an effect, which cannot be neglected – it's the skin depth. The penetration depends on difference in the synchronous angular velocity of the inductor and the melt's angular velocity ($\omega_0 - \omega$), the magnetic permeability (***μ***) and the electrical conductivity of the metal (***σ***). The equation is:

$$\delta = \sqrt{\frac{2}{\mu\sigma(\omega_0 - \omega)}} \tag{2}$$

The inductivity of the magnetic field decreases exponentially by the skin depth:

$$B = B_0 * e^{-d/\delta} \tag{3}$$

Where $B_0$ is the maximal inductivity of the field and ***d*** is the distance from the wall of the crucible. This equation was also used in the UDF to determine the magnitude of ***B*** correctly in every cell. The force filed was set as a tangential momentum. An example for the stirred gallium is shown on Figure 3 [1].

*Figure 3. Magnetically stirred liquid Ga-In alloy in D = 14 mm crucible*

## 3. Getting information from the model

The research group measured the average angular velocity of the melt. This data can be measured by two methods in the FLUENT.

First method is an average of the ratio of the tangential velocity (***v***$_t$) and the current radius (***r***) on a line (from the axle of the crucible to the wall) – equation (4).

$$\omega_{line} = \frac{v_t}{r} \tag{4}$$

Second is measured from the metallostatic pressure gradient. The gallium makes a potential vortex, and by this the pressure in the middle of the melt and at the wall is different. The liquid metal climbs up on the wall and the middle lowers. The average angular velocity can be computed from the distance of the lowest and the highest point of the melt according to equation (5) which has been derived from the general Bernoulli equation [1]. Figure 4 shows the empirical sketch for computing the angular velocity with eq. (5) from the distance between the high and low points (***2x***).

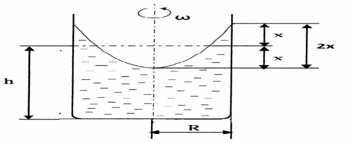

*Figure 4. Sketch for computing the angular velocity*

$$\omega_{press} = \sqrt{\frac{2 * 2x * g}{R^2}} \tag{5}$$

In Figure 4 the distance from the resting surface’s height (***h***) is the same upwards and downwards. Proved experimentally [2] and with the numerical simulations that, by the effect of wall friction, surface tension, surface wetting and others, the upper distance will be smaller and there’ll be a peak at the wall on the free surface, but the average angular velocity will also be smaller by this reason – also see Figure 3.

“2x” is easily accessible from coordinates of the interface between the gallium and the air. The anterior parameters were used to check the model’s validity. The real measured data from [1] and the computed FLUENT data were compared. The exact errors will be discussed later.

## 4. Results

### *4.1. Angular velocity – line method*

The model's running was checked by the plotting of the average angular velocity as a function of time on a line (from the axle of the system to the wall of the crucible). The plotted data is shown on Figure 5. "D10 B37" means 10 mm diameter crucible and 37 mT induction.

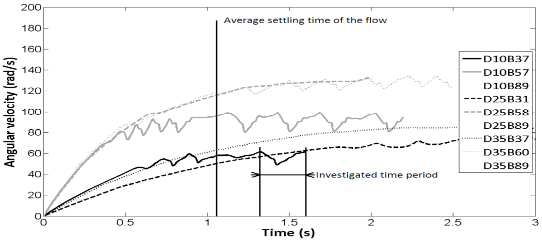

*Figure 5. Angular velocities as a function of time from 0 seconds*

The average settling times of the flows are at about 1.1 seconds. According to Figure 5, if the induction is the same, the values of the average angular velocity don't differ too much in higher diameters. An oscillating effect also can be seen on the curves. For the investigation of this effect see Figure 6, which shows the angular velocity measured from the axle to the wall of the crucible at 1.3, 1.4, 1.5 and 1.6 s of flow time. A difference can be found in the values nearby the wall, nevertheless the melt is faster near the axle.

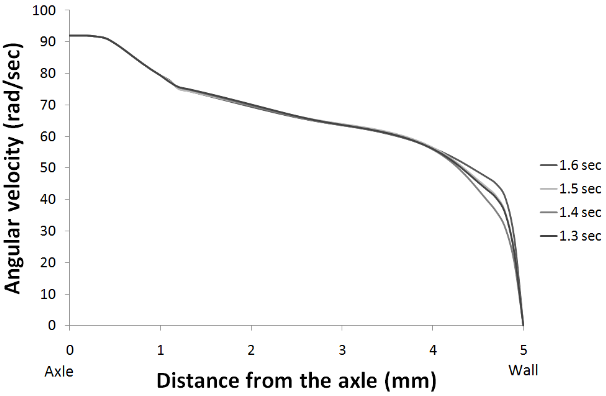

*Figure 6. Angular velocity plotted from the axle to the wall, D = 10 mm, B = 37 mT*

The form of the curve is similar in the 25 and 35 mm diameter, but the fastest point is at about the half of the radius – Figure 7. The reasons for the slowing effects and the peak on the higher diameters experiment's curve lie in the secondary flow of the melt. 10 mm and 35 mm diameters will be investigated. 25 and 35 mm cases show similar results.

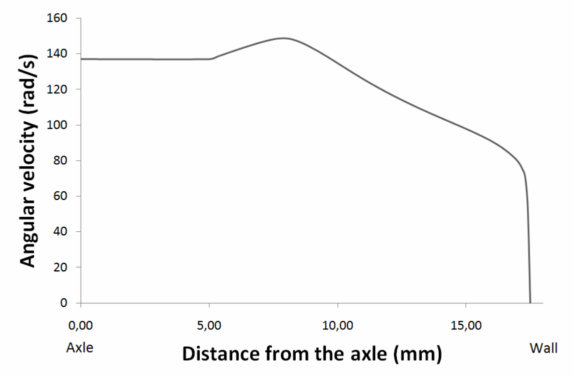

*Figure 7. Angular velocity plotted from the axle to the wall, D = 35 mm, B = 37 mT*

### 4.2. *Free surface, angular velocity – pressure gradient method*

The angular velocity data were also determined with equation (5). The lowest and the highest points of the free surface were measured for the calculations. Figure 8, shows the gallium's free surface at different inductions in 10 mm (a–c) and 35 mm (d–f) crucible.

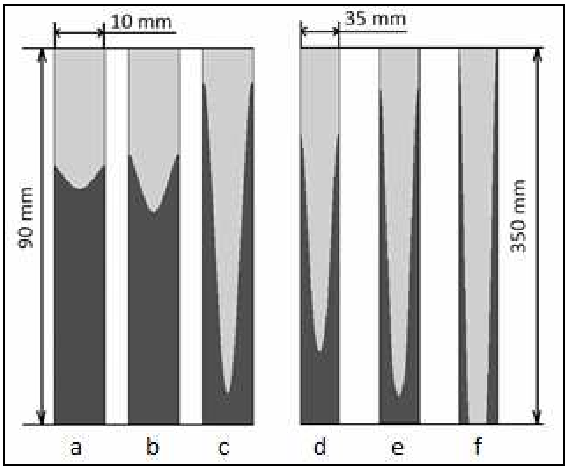

*Figure 8. Contours of Ga (dark phase), (a–c) D = 10 mm, (d–f) D = 35 mm*
*(a, d) B = 37 mT, (b, e) B = 57 mT, (c, f) B = 89 mT*

In the first approximation, the influence of the crucible's diameter is visible. As the diameter is getting higher, the depression on the free surface is getting stronger [1]. The case of figure 11f is not capable for pressure difference method, because the melt moved out to the wall and started rotating as a pipe.

### *4.3. Secondary flows*

As mentioned before, the angular velocity's is not constant in the whole volume of the gallium. In an empirical forced vortex, the angular velocity is constant all over the flow. According to figure 6, the angular velocity significantly reduces near to the wall. The depression in the value is caused by "near-wall effects". Figure 9a shows the secondary flows in the volume of the melt in the 10 mm crucible. 92% of the volume is making turbulent secondary flows and slowing down the melt's rotation at the wall. The other 8 V/V% of the gallium makes an updraft [3, 4], which has a significant role in the crystallization of other alloys – like Al-Si-Mg ternary – transporting the alloying particles thru the melt. Without stirring the particles' distribution is uniform [5].

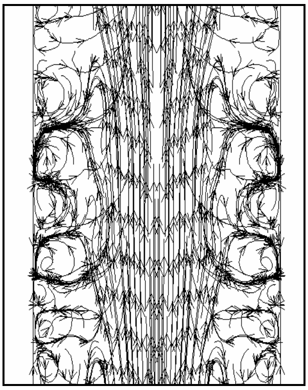

*Figure 9. a)*
*Pathlines of the secondary flow*
*D = 10 mm*

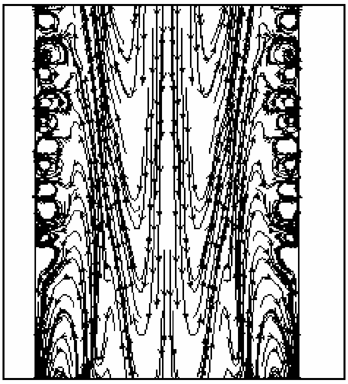

*Figure 9. b)*
*Pathlines of the secondary flow*
*D = 35 mm*

If the diameter of the crucible is bigger, the "near-wall effect" takes less action on the flow and less ratio – 46.5 V/V% – gets turbulent. The updraft is still visible, but in the middle of the "melt-cylinder" a downdraft appears. This movement feeds the updraft – see figure 9b. With 10 mm diameter there's not enough laminar zone to produce the downdraft. On account of the pressure difference between the middle and the edge of the melt, the updraft uses the whole laminar zone and the downdraft is forced out into the turbulent zone.

Figure 10. a)–10. d) show in order the gallium in the 10 mm crucible [scale bar shows the volume fraction of gallium, 10. a)], the contours of axial, radial and the tangential velocity [scale bar is in m/s, 10. b)–10.d)]. The turbulence is visible on all of the 3 velocity patterns and the contours of the tangential velocity [Figure 10. d)] proofs that the angular velocity decreases near the wall – see equation (4). Negligible amount of radial velocity's visible.

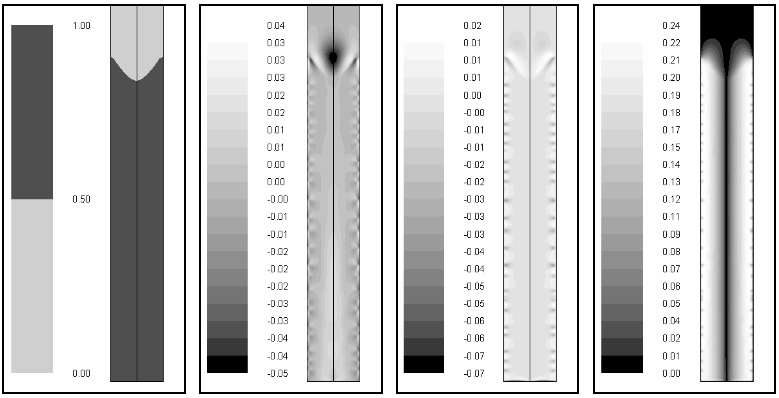

*Figure 10. a)* *Figure 10. b)* *Figure 10. c)* *Figure 10. d)*

*Contours of: **10.a**) volume fraction of gallium, **10. b**) axial velocity magnitude, **10. c**) radial velocity magnitude and **10. d**) tangential (swirl) velocity magnitude. Scale bar on **b) c)** and **d)** is in m/s; D = 10 mm, B = 37 mT*

The rate of the axial velocity in the updraft is 0.01–0.02 m/s. Compared to the tangential velocity – which's maximum is at about 0.22 m/s – the updraft is quite slow in the laminar zone, but can take enough action on the crystallization [4, 5].

Compared to the 35 mm diameter case [Figure 11. a)–11. d)], the axial velocity values change between 0.03–0.07 m/s. Negative value means downdraft and it seems to be double stronger than the updraft. The reason of the faster flow might be the smaller "flow cross-section" in the middle or that the turbulences don't affect the flow. The gravity can also cause difference. If the gravity is turned off in the model, the melt can "climb out" from the crucible. The velocity contours would be different too.

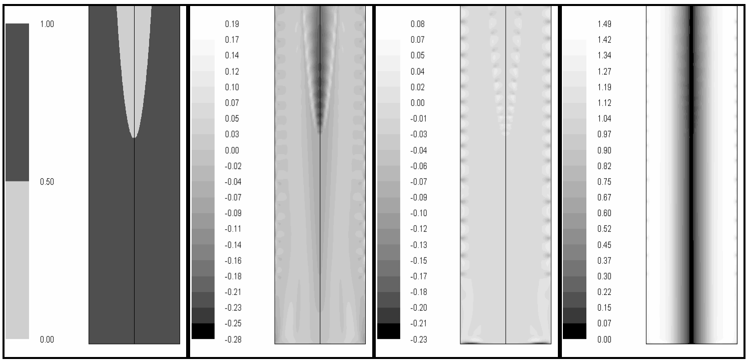

*Figure 11. a)* *Figure 11. b)* *Figure 11. c)* *Figure 11. d)*

*Contours of: **11. a**) volume fraction of gallium, **11. b**) axial velocity magnitude, **11. c**) radial velocity magnitude and **11. d**) tangential (swirl) velocity magnitude. Scale bar on **b) c)** and **d)** is in m/s; D = 35 mm, B = 37 mT*

Radial and tangential velocity distributions are similar to the 10 mm diameter one, but with different values and smaller area of turbulence. The tangential velocity's maximum is 1.5 m/s – see figure 10. b)–d) It's 625% of the tangential velocity maximum in the 10 mm crucible. The peak on the curve of figure 7 is caused by the effect of the axial velocity distribution. The fastest updraft and the peak appear at the half of the radius. The same peak appears in case of 10 mm, and also at the same place where the updraft is – in the middle of the melt. Less weakening is affected on the primary flow by these laminar zones and higher angular velocities can be reached.

Spiral flow lines can be found on the surface of the gallium on Figure 3 [1]. Those spirals are caused by the amount of the primary rotational flow and the (secondary) updraft (or any axial flow), which is occurred by the pressure difference in the melt.

## 5. Errors of the model

The measured data of Rónaföldi [1] for the angular velocity was used for validation of the model. The relative errors of the average angular velocity (from both line and pressure difference methods) are shown on Figure 13. a). The errors of the sedimentation are shown on figure 12. With line method, the angular velocity's error is average of 8% in 10 mm and 19.8% in 35 mm. With pressure method, this data is 14.1% in 10mm and 46.6% in 35 mm.

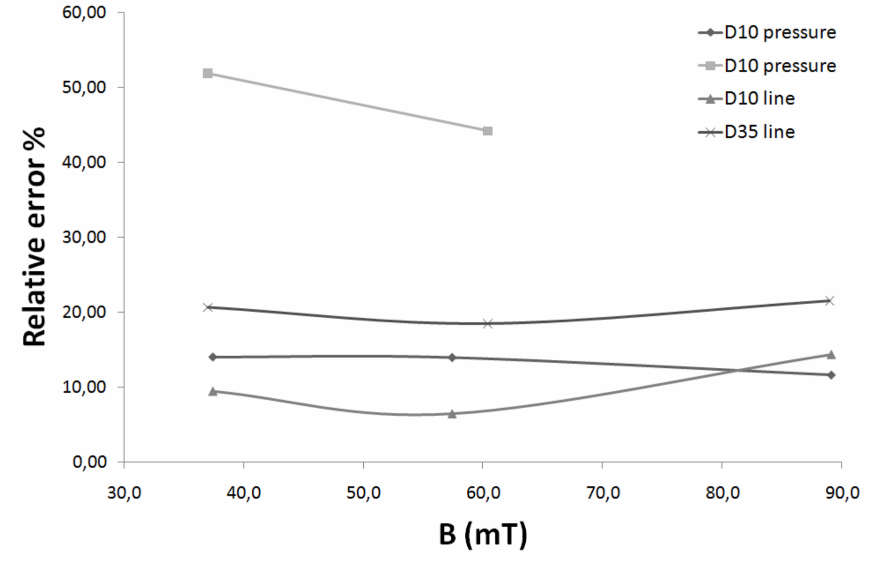

*Figure 12. Relative error on the angular velocity measured with both methods as a function of the induction*

## Conclusions

A model for investigating the hydrodynamic properties of a Ga-In alloy during magnetic stirring was made. The Lorenz force field, which is rotating the melt, was programmed with User Defined Functions.

Two methods for measuring the angular velocity in the melt were used. The "line method" is appropriate to check the model during running and to measure the distribution of the angular velocity across the radius. The "pressure gradient method" is a faster technique for gathering averaged values and also handy to measure in any moment of the flow time – the oscillating effect in the "line method" (see Figure 5) can be eliminated. With line method, it's difficult to decide the time of measurement.

In the future a more detailed flow inspection could be useful and the turbulent model can be a good base for solidification modeling.

### Acknowledgements

*This research was made as part of TÁMOP-4.2.1.B-10/2/KONV-2010-0001 project in the framework of the New Hungarian Development Plan.*

### References

[1] Rónaföldi, A.: *Forgó mágneses mezős magneto-hidrodinamikai keverővel ellátott kristályosító berendezés kifejlesztése és vizsgálata*. Miskolc, 2008.

[2] Rónaföldi, A.–Roósz, A.–Kovács, J.: *The influence of surface roughness of crucible's wall on the flow rate of melt stirred during solidification*. The 3rd International Conference on Advances in Solidification Processes, 2011.

[3] Budenkova, O.–Baltaretu, F.–Kovács, J.–Roósz, A.–Rónaföldi, A.–Bianchi, A-M.–Fautrelle, Y.: *Simulation of a directional solidification of a binary Al-7wt%Si and a ternary alloy Al-7wt%Si-1wt% Fe under the action of a rotating magnetic field*. In press.

[4] Zimmermann, G.–Weiss, A.–Mbaya, Z.: *Effect of forced melt flow on microstructure evolution in AlSi7Mg0.6 alloy during directional solidification*. Materials Science and Engineering A 413–414., 236–242., 2005.

[5] Kovács, J.–Rónaföldi, A.–Roósz, A.: *Effect of the High Rotating Magnetic Field (min. 30 mT) on the Unidirectionally Solidified Structure of Al7Si0.6Mg Alloy, Mater*. Sci. Forum Vol. 649, pp. 263–268., 2010, doi:10.4028/www.scientific.net/ MSF.649.263

*Materials Science and Engineering, Volume 38/1. (2013), pp. 51–59.*

# INVESTIGATION OF THE PORE DISTRIBUTION PARTS OF THICK-WALL CASTINGS BY COMPUTER IMAGE ANALYSIS

MÓNIKA TOKÁR[1]–JENŐ DÚL[2]–TAMÁS MENDE[3]

Nowadays, one of the most up to date and dinamically developing measuring/evaluation possibility is the computer image analysis. We determined the pore distribution on microscope photos by using image analysing to study the failures of the thick-wall high pressure die castings.

**Keywords:** high pressure die casting, image analysis, inhomogeneous.

## Introduction

In case of not suitable casting geometry and technical parameters the thick-wall parts include an inhomogeneous inside zone and a fail-safe outside skin (Figure 1). In the interest of availability we can refine just the outside skin, because just this layer has good mechanical properties. In our work we produced and analysed different thickness experimental casting and analysed a real industrial casting. After sample polishing we made a series of microscopy pictures from the one side to the other side in the function of the wall-thickness. We measured the pore size in every picture and measured the pore distribution in the function of the wall-thickness by using a computer image analysing method. We compared the inside and the other side parts.

In case of expressly thick-wall high pressure die castings, the not perfectly elected castings geometry and technological parameters cause formation of two layers during the solidification. The outside quickly-solidifying layer is pore-free, but the inside inhomogeneous part includes a lot of – various sizes – pores. This inhomogeneous structure causes errors at mechanical machining process, therefore the machining depth can not be deeper than the outside pore-free layer. For the required mechanical properties, it is very important that this external pore-free layer should not be removed. In the factories the internal inhomogeneous structure is examined by various metallographical methods, so our purpose was defining a pore distribution in the function of the wall-thickness. A lot of large pores in the internal part cause often too much waste. In our work we produced and analysed different thickness experimental castings and analysed a real industrial casting. We cut samples from predetermined parts of the castings, and after sample polishing we made a series of microscopy pictures from the one side to the other side in the function of the wall-thickness. The wall-thicknesses of the castings were the followings: experimental casting: 4 mm, 8 mm, 12 mm; industrial casting: 13 mm. We compared the pore-free

---

[1] University of Miskolc, Metallurgical and Foundry Engineering Institute
3515 Miskolc-Egyetemváros, Hungary
monika.tokar@uni-miskolc.hu
[2] University of Miskolc, Metallurgical and Foundry Engineering Institute
3515 Miskolc-Egyetemváros, Hungary
[3] Hungarian Academy of Science, Materials Science Research Group
3515 Miskolc-Egyetemváros, Hungary

external and the pore-rich internal zone, and we analysed the transitional zone between them. The microscopy picture series were evaluated by computer image analysing method in function of the wall-thickness. We investigated particularly the amount of the pores (largest pore diameter of every pore), the statements were taken by right of pore-criteria), and we made pore distribution diagrams in function of wall-thickness.

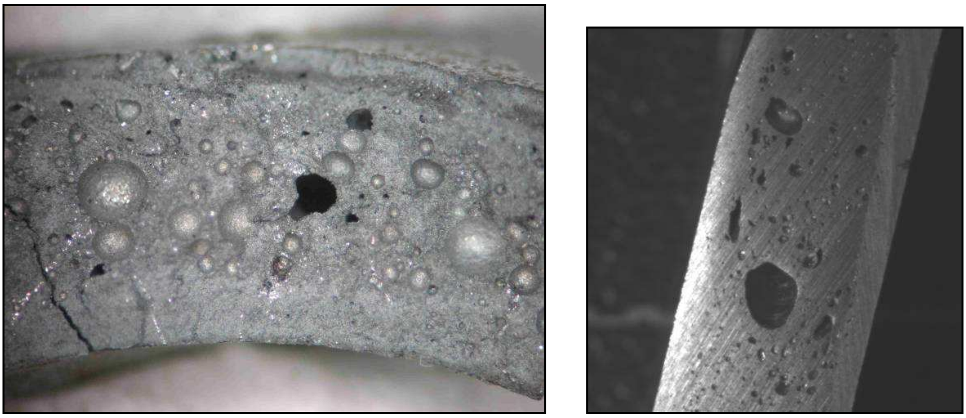

*Figure 1. Inhomogeneity in internal zone (broken surface and polished surface)*

## 1. Metallographical analysing of pore distribution in high pressure die casting

### *1.1. Measuring of pore volume by computer image analysing*

We photographed the structure of sample in every field of view from one side to other side of the casting in function of wall-thickness. The current wall-thickness (4, 8, 12, 13 mm) can be covered by 7, 14, 19, 25 fields of view at 200x magnification. We used a qualified microscope to take these picture series.

This microscope (according to applied computer software) prepares the picture series automatically (from the left side to the right side of the sample – Figure 2). Before picture taking, you can set optional focus points on the surface of the sample in order to high quality and well focused pictures in every field of view. The computer generates a net which can help you to do this step of setting. After the settings, you can start the program of the microscope. The pieces of picture series were evaluated by using image analysing software, analysing the pictures one by one. The used “Cprob” image analyser software was developed by Péter Barkóczy (University of Miskolc, Materials Science Institute).

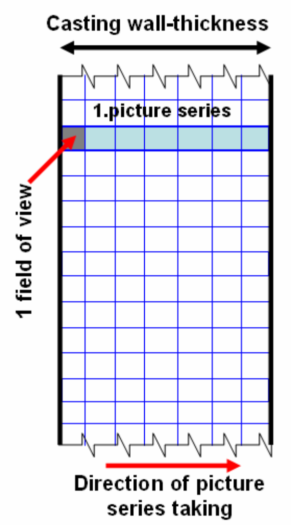

*Figure 2. The steps and directions of picture series taking*

The evaluating steps of the analyser software (Figure 3–4):

**1. Image acquisition** → **2. Digitising the grey image** → **3. Digital processing of grey images** → **4. Segmentation (detection)** → **5. Transformation of binary images** → **6. Measurement, obtaining the measurement results** →
**7. Interpretation of measurement results** [1.]

**1. Image acquisition:** Taking the images in electronic form by a suitable instrument, which can be a video camera mounted on a light microscope, or electron microscope.
**2. Digitising the grey image:** Adaptation of the different grey level to each of the intensity values of image colours.
**3. Digital processing of grey images:** Emphasising the features or objects to be investigated, i.e. separating the essential and less essential information.
**4. Segmentation (detection):** The complete separation of objects and background on the basis of one of their properties (e.g. their grey level, shape or orientation) as a result of which a binary image develops.
**5. Transformation of binary images:** Performing of binary transformations, i.e. the transformation of objects such a way, that they can approximate their ideal shape in the most optimal way (e.g. separation of grains which seem to be coalesced in the image but they are separated in the reality), preparation of measurement.
**6. Measurement, obtaining the measurement results.**
**7. Interpretation of measurement results:** In the materials science the results are interpreted on the basis of different microstructure models by using the stereological knowledge.

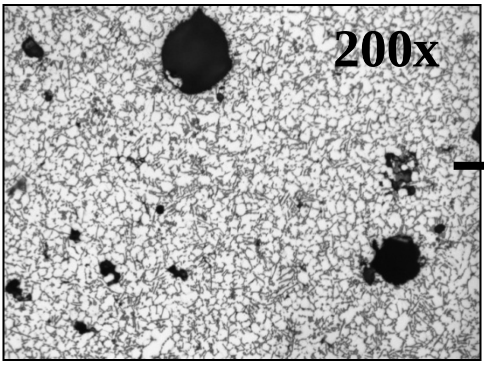

*Figure 3. Original microscopical picture*

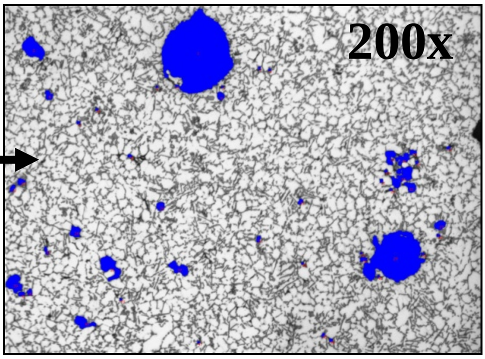

*Figure 4. Modified binary picture*

On Figure 5. and Figure 6. you can see two examples of the prepared microscopy pictures, one from the internal (pore rich) layer, and one from the external (pore free) layer of casting.

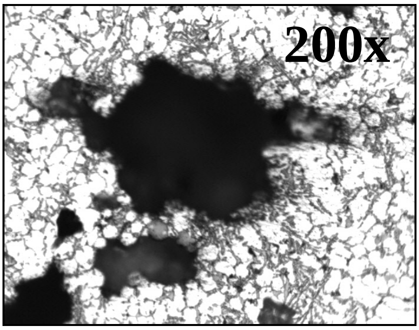

*Figure 5. Microscopical picture from the internal layer*

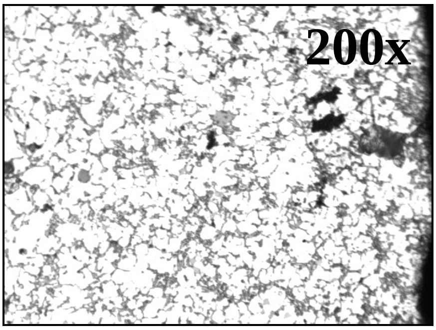

*Figure 6. Microscopical picture from the external layer*

The stated pore-requirements in front of the castings are determined by the hard specifications of the customers. We have to define some criteria to decide that the casting is adequate or not. Customers categorize the maximal acceptable diameter of pores, the minimal distance between two pores, and the negligible diameter of pores (Table 1) [2]. We made our metallographical measurements by using these standards. We compared our results with these values in case of every wall-thickness. We grouped our values as (1) smaller than the margin of error, and (2) larger than the margin of error, it can be shown well on chart in the function of wall-thickness.

*Table 1*

*The applied pore-criteria*

| **Pore-/ Shrinkage category** | **Pore-/Shrinkage-diameter/ max. range** *d (mm)* | **Pore-/ Shrinkage distance** *a min. (mm)* | **Below the margin of error Pore/Shrinkage – diameter Ø** *d(mm)* |
|---|---|---|---|
| P1 | 0,1 ≤ d ≤ 0,15 | 3 | < 0,1 |
| P2 | 0,15 ≤ d ≤ 0,25 | 4 | < 0,15 |
| P3 | 0,2 ≤ d ≤ 0,5 | 4 | < 0,2 |
| P4 | 0,4 ≤ d ≤ 1,0 | 2 | < 0,4 |
| P5 | 0,6 ≤ d ≤ 2 | 3 | < 0,6 |

### *1.2. Pore volume measuring by computer image analysing method*

We used terraced-shaped experimental casting, there were 3 different wall-thicknesses, 4 mm, 8 mm and 12 mm, the surface of these parts were 100x200 mm. Our aim was determining the pore volume distribution in the function of wall-thickness, and investigating how thickness causes the appearance of the internal inhomogeneous zone. In case of high pressure die casting, the 4 mm wall-thickness is a normal/thin thickness, the 8 mm wall-thickness is a normal ordinary size, but the 12 mm is already thick. We have taken microscopical picture series from every sample, and 1 rows of the picture series were evalueted by image analyser software. (We made parallel measurings in order to high quality results.)

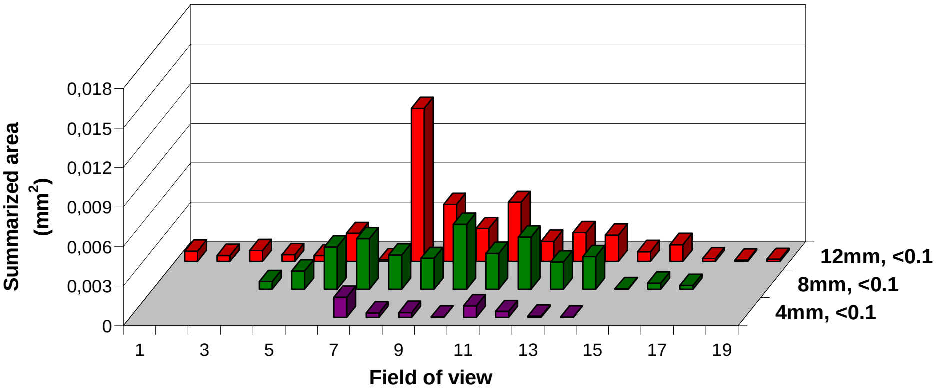

*Figure 7. a) The summarized area of pores in function of wall thickness per field of view – smaller pores than the margin of error*

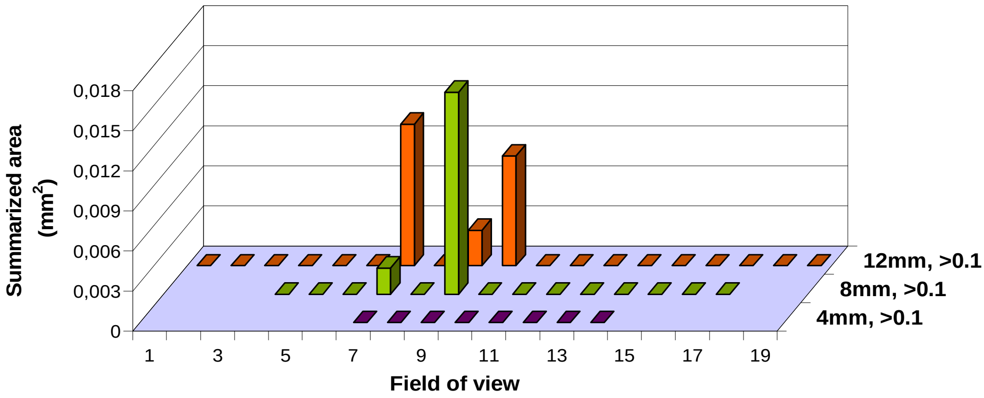

*Figure 7. b). The summarized area of pores in function of wall thickness per field of view – larger pores than the margin of error*

In Figure 7. a)–b) we differentiated our results as (1) smaller pores than the margin of error (<0.1 mm), and (2) larger pores than the margin of error (>0.1 mm). In case of the 4 mm thickness (7 fields of view) it can be seen that there is no pore above the margin of error. In case of the 8mm thickness (14 fields of view) there are already some pores above the margin of error, especially in the internal zone. The results of the 12 mm thickness (19 fields of view) show well that larger pores (which are above the margin of error) are located only in the internal zone, the external layer is free from larger pore. The summarized area of pores shows that the pores which are below the margin of error may have larger summarized area than all pores above the margin of error.

It can be see well in Figure 8 (picture from 4 mm wall-thickness sample) that the pores are mainly pores between the dendrite arms or smaller air inclusions.

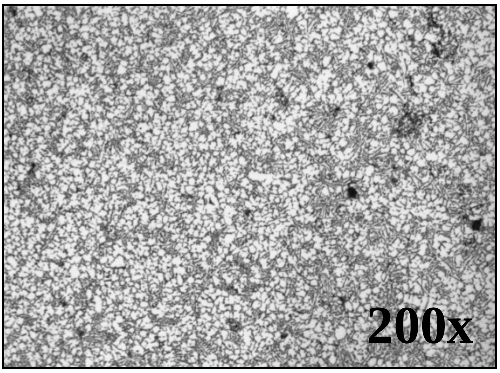

*Figure 8. Microscopical picture from the surface of the 4 mm wall-thickness sample*

In Figure 9, larger pores are appearing by increasing the wall thickness (8 mm), characteristically in the internal parts of the specimen.

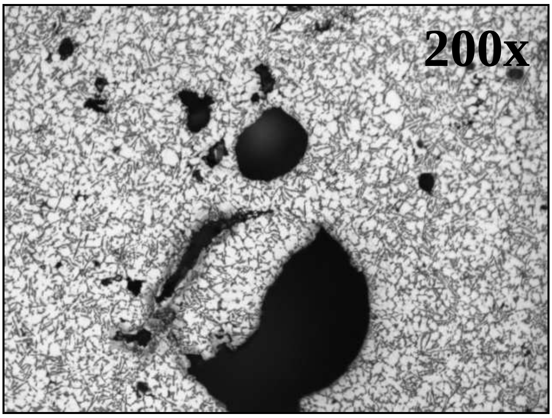

*Figure 9. Microscopical picture from the surface of the 8mm wall-thickness sample*

In Figure 10, there are too large pores in 12 mm wall-thickness sample, mainly in the internal layer.

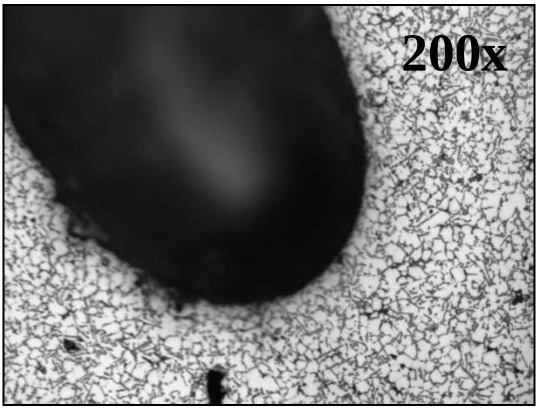

*Figure 10. Microscopical picture from the surface of the 12 mm wall-thickness sample*

### 1.3. Results of the real industrial high pressure casting

We cut samples from an automotive casting thick-wall (13 mm) part, the samples were polished and prepared to the measurements. We made a series of microscopical pictures (in the same way as the previous part of our work), and its 3 rows were evaluated by image analyser software. We differentiated 3 different rows, because this part of the casting has two boreholes, which can cause formation of heat-aggregation zone. The "row no. 1" and the “row no. 3” mean the rows near the borehole, and the “row no. 2” means the row away from the borehole. Our aim was determining the pore volume distribution in function of the wall-thickness.

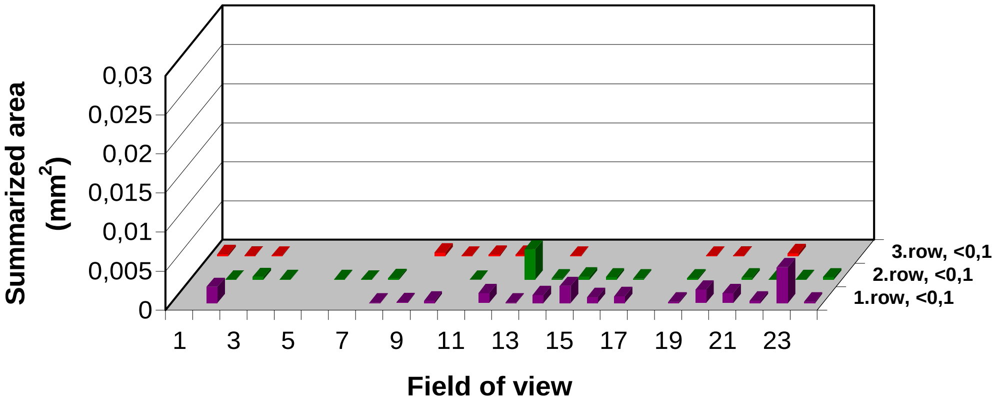

*Figure 11. a) The summarized area of pores in function of wall thickness per fields of view – smaller pores than the margin of error*

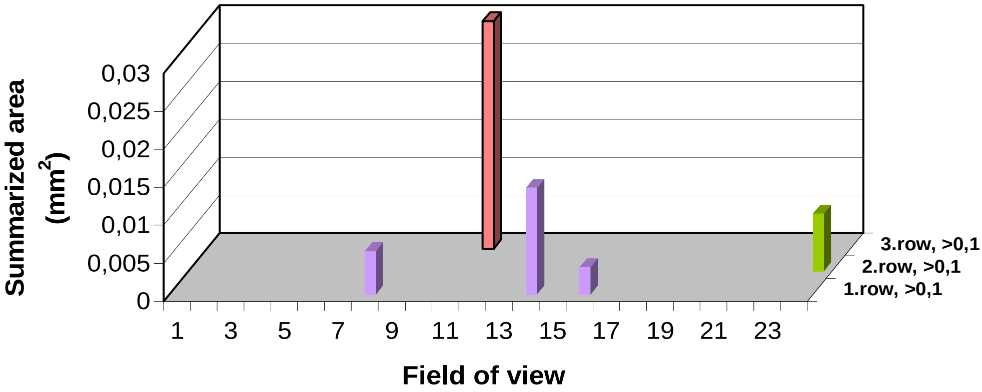

*11.b Figure 11. b) The summarized area of pores in function of wall thickness per fields of view – larger pores than the margin of error*

As you can see, in Figure 11. a)–b) we differentiated the pores as smaller than the margin of error (<0.1 mm), and larger than the margin of error (>0.1 mm). It can be established that the industrial casting has less failure than the experimental casting. The casting with adequate casting technology causes these better results. It should be noted, that the places of occurrence of pores in this examined industrial casting are not so obvious like in case of the previous examined experimantal casting.

We show the different types of pores in internal and in external layers of the casting in Figure 12–13.

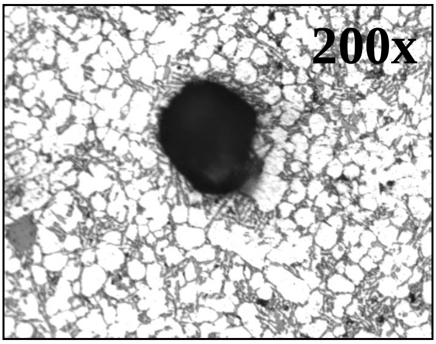

*Figure 12. Microscopical picture from internal part*

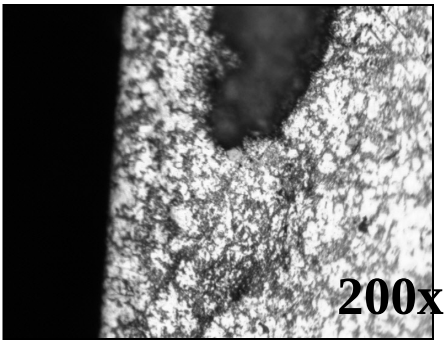

*Figure 13. Microscopical picture from external part*

## Conclusion

After the image analysing it can be established, that in case of 4 mm (normal/thin) wall-thickness there are no pores typically above the margin of error. Larger pores appear in case of 8 mm and 12 mm (normal or thick wall-thickness), the pores above the margin of error are mainly in the internal zone. The investigation of the industrial casting (13 mm wall-thickness) shows that there are less large pores than in case of the experimental casting. It means, that you can handle the thicker casting with adequate casting technology and adequate shape of casting. If the parameters of the casting is not enough precise, the pores will appear by the way of a determinable distribution in function of the wall-thickness.

We established the computer image analysing method and the application of the shown pore distribution analysing are suitable for qualification of experimental and industrial castings by right of pore content. Using the pore distribuiton charts it can be seen which part of the casting has too much and too large pores. These parts which includes the pores above the margin of error should be handled by changing of the casting parameters or – in case of serious cases – changing of the casting geometry.

### Acknowledgement

*The described work was carried out as part of the TÁMOP-4.2.1.B-10/2/KONV-2010-0001 project in the framework of the New Hungarian Development Plan. The realization of this project is supported by the European Union, cofinanced by the European Social Fund.*

### References

[1] Gácsi, Z.: *The Application of Digital Image Processing for Materials Science*. Materials Science Forum,Vol. 414–415., pp. 213–220., 2003.

[2] *Bildreihentafel für Poren und Lunker bei Druckgußteilen*. Werk-Normen 911 504 6554, WABCO Automotive Products Group

[3] Gácsi, Z.–Sárközi, G.–Réti, T.–Kovács, J.–Csepeli, Zs.–Mertinger, V.: *Stereology and Image Analysis.* WellPRess PHARE, Miskolc, 2001.

*Materials Science and Engineering, Volume 38/1. (2013), pp. 61–71.*

# EXPERIMENTAL INVESTIGATION OF ZINC PRECIPITATION FROM EAF DUST LEACHING SOLUTIONS

TERÉZIA VARGA[1]–TAMÁS I. TÖRÖK[2]

Steel scrap recycling in electric arc furnaces (EAF) is accompanied with relatively great amounts of dust generated which contains high percentages of zinc oxides and iron oxides together with several other chemical compounds. In principle, extraction of zinc from such dusts could be envisaged by several hydrometallurgical routes with using different selective leaching, then precipitating agents. In this preliminary laboratory experimental work the major conditions of zinc precipitation from zinc containing aqueous ammonia ammonium carbonate solutions were examined. Real leached liquors obtained from the industrial EAF dust (Bous, Germany) REDILP leach-grinding experiments as well as aqueous ammoniacal zinc solutions prepared from pure chemicals (so-called model system) were tested in stirred laboratory precipitation reactors equipped with dosing inlets to supply and dissolve gaseous $CO_2$ as a precipitation agent. The higher temperature precipitation technique of water steam distillation was also examined in some additional laboratory experiments and its feasibility was also proved for removing the rest of dissolved zinc from such solutions.

**Keywords:** leach-grinding, zinc, precipitation, ammonia-ammonium carbonate.

## Introduction

Secondary steelmaking in mini-mills is one of the main processes developed for steel scrap recycling where the scrap is usually melted in an electric arc furnace (EAF). During the melting process relatively high amounts of EAF dust is generated, which contains significant amounts of zinc, iron, lead, calcium etc., due to among others the prior anticorrosive treatments of many steel products [1]. The phase composition of the EAF dust is also rather complex: along with several simple metal oxides there is a significant amount of poly metallic oxides, the so called ferrites (spinels) which are thermodynamically rather stable. This complex composition is the main reason why EAF dusts are difficult-to-treat wastes. Nevertheless, the high metallic content of such wastes predestines their recycling instead of land-filling.

Within the framework of the "REDILP" EU6 project (Recycling of Electric Arc Furnace (EAF) Dust by Integrated Leach-grinding Process) and a MÖB-DAAD bilateral project, it was aiming at developing the technological fundamentals of an environmentally sound, economical and waste free process for treating EAF in order to be able to recover the heavy metals by a closed-loop, mechanically activated leaching process [2]; and to optimize the recovery and improve the products quality as much as possible.

---

[1] University of Miskolc, Institute of Raw Materials Preparation and Environmental Processing, Faculty of Earth Science and Engineering
3515 Miskolc-Egyetemváros, Hungary
ejtvater@uni-miskolc.hu
[2] University of Miskolc, Institute of Metallurgy and Foundry Engineering, Faculty of Materials Science and Engineering
3515 Miskolc-Egyetemváros, Hungary
fektt@uni-miskolc.hu

As a small part of the above mentioned international joint REDILP project [3], the present paper deals with the experimental investigation of the recovery of zinc from EAF dust by means of precipitation and steam distillation from ammonia-ammonium carbonate leaching solutions.

## 1. Recovery of zinc from solutions

Production of zinc oxide from residues of scrap recycling operations by means of the ammonia-ammonium carbonate system has been previously reviewed [3–7]. In principle, this selective leaching technique could be applied to different zinc containing metallurgical wastes like drosses, ashes, bag dusts and sludge from zinc galvanizers and various other operations. Although there are several other leaching agents as well for zinc, but the aqueous solutions of ammonia and ammonium carbonate seems to possess the most desirable combination of properties. They are relatively cheap and easily recoverable, and the dissolved zinc can be precipitated in the form of simple compounds from which, if necessary, even metallic zinc can be easily obtained by extractive metallurgical reductive techniques like aqueous electrowinning.

Working with aqueous ammonia-ammonium carbonate leaching solutions, the dissolved zinc can then be precipitated in several low solubility products as for example zinc hydroxide, carbonate or basic zinc carbonate. However, there are several technological parameters which must be properly set and controlled during precipitation from such Zn containing liqours. Hence, in the course of our laboratory investigations the following main targets were aiming at:

- Determining the limiting parameters of the hydrometallurgical zinc recycling process using ammonia-ammonium carbonate leaching solution to recover zinc;
- Setting up the framework of further research to develop an optimized flow sheet for the economical hydrometallurgical treatment of Zn containing EAF dusts.

## 2. Experiments on the zinc precipitation from the real EAF dust leaching solutions

The precipitation experiments were carried out in the laboratories of the project-partners both at Otto von Guericke University Magdeburg, Germany and at University of Miskolc, Hungary. The Zn containing leached solutions were produced in a laboratory reactor by using the REDILP leach-grinding technique [8] on real industrial EAF dust samples received from the Bous Steel Mill in Germany, the phase composition of which is presented in Table 1.

*Table 1*

*Major phases / components of the tested EAF dust in mass percentages*

| **EAF dust from Bous (steel works, Germany)** | | | |
|---|---|---|---|
| Franklinite/$ZnFe_2O_4$ spinel/ | 49.5 % | Hematite /$Fe_2O_3$/ | 7 % |
| Magnetite /$Fe_3O_4$/ | 10.5 % | Rest (mostly other oxides) | ~ 4 % |
| Zincite /ZnO/ | 29 % | | |

Primary aim of the laboratory experiments was to determine the parameters at which the zinc recovery rate from the leached solution is the highest. For the precipitation of zinc the properly filtered solution was fed to the precipitation apparatus shown in Figure 1.

*Figure 1. Photograph of the precipitation apparatus equipped with a mechanical stirrer, a $CO_2$ gas supply unit, and sensors to measure the solution conductivity, pH and temperature*

While supplying and dissolving $CO_2$ in the zinc containing ammonia-ammonium carbonate leached solutions, in principle, the following precipitation reaction should take place with the formation of solid precipitates of zinc hydroxide and zinc carbonate:

$$2[Zn(NH_3)_4]^{2+} + 4H_2O + CO_3^{\,2-} \leftrightarrow Zn(OH)_2 \cdot ZnCO_3 + 4NH_4^{\,+} + 2OH^- \tag{1}$$

During the first six experiments the precipitation reactor was set to work at room temperature, that is without controlling its temperature at any pre-set value, and only the stirring speed and the volume flow rate of $CO_2$ were chosen as varying parameters (Figure 2). In Figure 2 it is seen that there were relatively significant increases of the solutions/suspensions temperatures in the course of precipitations partially due also to the exothermic nature of the formation of solid zinc carbonate:

$$Zn^{2+}(aq) + CO_3^{\,2-}(aq) \rightarrow ZnCO_3(s) \tag{2}$$

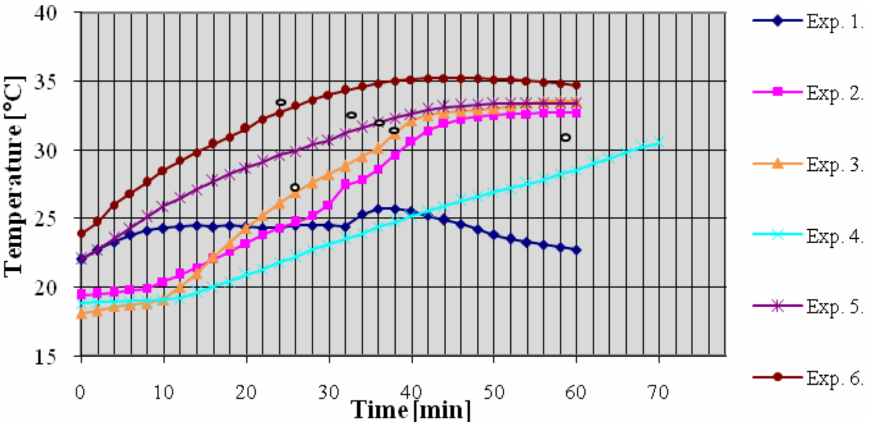

*Figure 2. Changing of temperature in the first six precipitation experiments with $CO_2$ addition to the leached liquors at different volume flow rates and stirring speeds (exp1.:$CO_2$ 5L/min, 700rpm, exp.2.: $CO_2$ 5L/min, 1000rpm, exp.3.: $CO_2$ 5L/min, 1400rpm, exp.4.:$CO_2$ 1L/min, 700rpm, exp.5.: $CO_2$ 7L/min, 700rpm, exp.6: $CO_2$ 10L/min, 700rpm)*

The small open circles in Figure 2 indicate those approximate residence times when the first observable signs (in turbidity) appeared. Prior to that there is the aqueous dissolution of $CO_2$ followed by the nucleation of the precipitates from the (over)saturated liquors. This initial period was the longest (62 min) when the $CO_2$ supply was the slowest at a stirring rate of 700 rpm (exp. 4.). Otherwise, in all the other cases the first deposits appeared after about 20 to 35 minutes. After each experiment the precipitates were removed by vacuum filtration and sent to chemical analysis in order to determine the recoveries of the metals (Zn and the co-precipitated other ones (Fe and Pb) in the solid products.

In *Figure 3* the changing of pH in the liquid phase is shown in the function of time with constant volume flow rates of $CO_2$ supply. It can be seen in *Figure 3* that the pH values were decreasing in all the cases (exps. 2, 4, 5 and 7) depicted here, because of the hydrolysis reaction of $CO_2$ gas with the formation of the weak acid of $H_2CO_3$ in the solution together with its dissociation products ($HCO_3^-$ and $CO_3^{2-}$) which, at least partially, are capable to replace the complexing molecules of $NH_3$ being coordinated around the $Zn^{2+}$ cations, and so enforce the formation of the insoluble precipitates of zinc carbonates. Liberating out from the coordination spheres of $Zn^{2+}$ cations, the so disengaged molecules of ammonia in solution can then get combined with the dissolved molecules of $CO_2$ (in an aqueous neutralization reaction), hence in the course of the pH curve there appears an inflexion point after which the pH approaches constant values at around 8.2 to 8.5 depending also on some other conditions of the experiments.

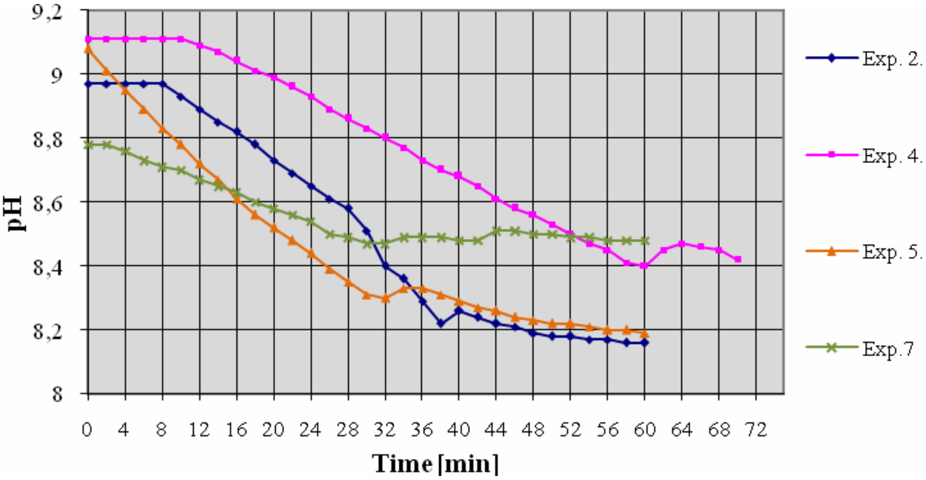

*Figure 3. Changing of pH during precipitation with $CO_2$ addition (exp.2.: $CO_2$ 5L/min, 1000rpm; exp.4.:$CO_2$ 1L/min, 700rpm; exp.7.: $CO_2$ 5L/min, 700rpm; exp.5.: $CO_2$ 7L/min, 700rpm,)*

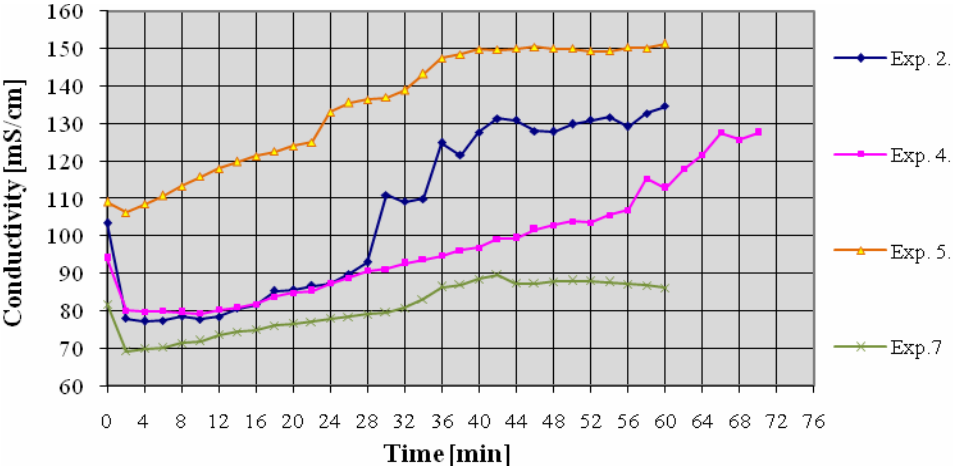

*Figure 4. Changing of solution conductivity during precipitation with $CO_2$ addition (exp.2.: $CO_2$ 5L/min, 1000rpm, exp.4.:$CO_2$ 1L/min, 700rpm, exp.5.: $CO_2$ 7L/min, 700rpm, exp.7.:$CO_2$ 5L/min, 700rpm)*

During the precipitation experiments the electrical conductivities of the zinc containing liquors were also recorded and their increasing tendencies are clearly seen in *Figure 4* for all the systems illustrated here. In the initial periods it can be explained with the increasing number of free ionic species due to the dissolution of $CO_2$, and the inflexion points can then be associated with the appearance of new phases.

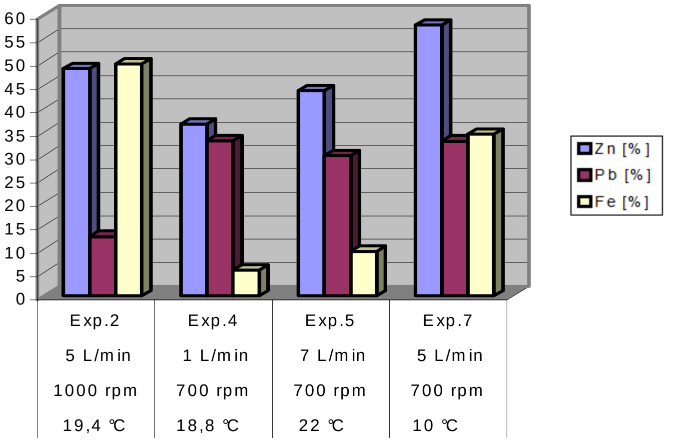

*Figure 5. Recovery rates (in wt.%) of the three major metallic constituents (Zn, Pb, Fe) of the precipitates obtained by $CO_2$ addition to the leached liquors*

In *Figure 5* the recovery rates of zinc and two other major contaminating co-precipitated metals (lead and iron) are also shown together with the principal experimental conditions. And, it should be noted here, that though the ammonia-ammonium carbonate leach-grinding digestion procedure was found really highly selective for the solubilization of zinc, but still some varying amounts of other metals (<2% of Fe and 2 to 50% of Pb etc.) went also into the leached liquors. Moreover, as the recovery rates of zinc with $CO_2$ precipitation was also found not high enough (between 37 and 58%), hereinafter, we have tried to reveal the reason by designing and performing further laboratory experiments based on so-called model aqueous solutions prepared from pure chemical compounds of the leaching agents and that of zinc.

## 3. Zinc precipitation experiments from model solutions

From the several metals present in the EAF dusts and more or less soluble in ammonia-ammonium carbonate leaching solutions, only the zinc was selected for the preparation of the model solutions, which were prepared in similar concentration ranges to the ‘real’ ones described above. It was also aiming at here to determine the highest achievable metal recovery values in the precipitates for zinc.

Therefore, another set of precipitation experiments was designed with model solutions and carried out using another apparatus which was constructed at the Department of Non-Ferrous Metallurgy, University of Miskolc, based on the installation used in Magdeburg

(Figure1). The model solutions had the following initial concentration: c/$NH_4OH$/ ≈ 3,9 mol/$dm^3$; c/$(NH_4)_2CO_3$/ ≈ 2,7 mol/$dm^3$; c/ZnO/ ≈ 0,9 mol/$dm^3$. The $CO_2$ set flow value was 4 L/min, the stirring rate was 400rpm and the temperature was varied (12, 20 and 40 °C). Temperatures and pH values inside the reactor were recorded by an NI DAQ-6008 USB data collector module. After about 2.5 hours of experimenting (residence time for precipitation) the solid phases were separated from the liquid by vacuum filtration, then the liquid portions were chemically analyzed by atomic absorption spectrometry.

*Figure 6. The home-made precipitation reactor assembled at the Department of Non-Ferrous Metallurgy at University of Miskolc*

Again, quite many sets of experiments were done of which only the results of the most representative ones are illustrated here and compared with those obtained during the precipitation experiments with the real EAF dust leaching solutions. In the case of the model solutions the pH values of precipitation was measured in between 8.4–9, which range is very close to the 8.2–8.6 found for the real solutions. Here as well the curves depicting the values of pH *vs*. time (Figure 7) showed some kind of inflexion points which are also associated with the appearance of a new phase in the model systems.

Working with the model solutions, the percentage values of zinc recovery were as low as 20…38%, while the same recovery values were around 37…58% in the case of the real solutions. This latter higher recovery rates can be explained by the differences in the design and construction of the two laboratory precipitation reactors as for example the supply of $CO_2$ gas could not be so well and homogenously dispersed with the home-made Miskolc apparatus as with the more professional one used previously in Magdeburg. Another probable reason of the somewhat higher zinc recoveries found in cases working with real solutions might be the co-precipitation reactions of the other metals present in the real liquors obtained after leach-grinding of the industrial EAF dust samples.

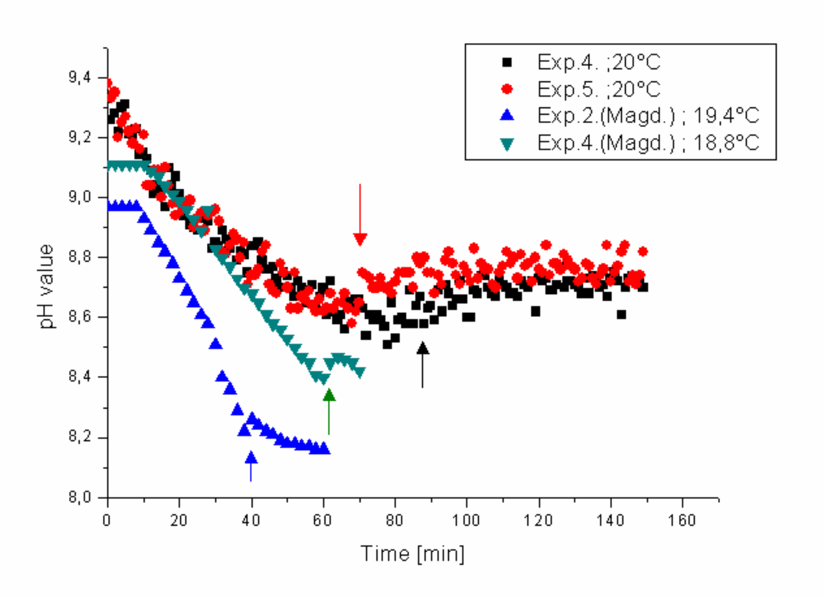

*Figure 7. Changing pH values during the course of precipitation both with model solutions (Exp. 4 and 5) and the "real" ones obtained by EAF dust leaching [Exp. 2 (Magd) and Exp. 4 (Magd.)]*

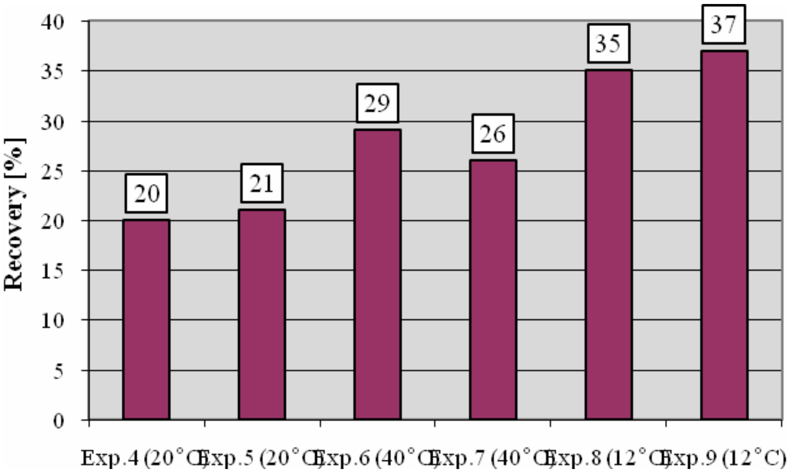

*Figure 8. Zinc metal recovery rates (in wt.%) obtained with $CO_2$ precipitation from model solutions prepared from pure chemicals of zinc ammonia and ammonium carbonate in water*

In the course of the successive precipitation experiments on model solutions we were able to improve the technique of $CO_2$ supply, hence its dispersion efficiency as well, and it must have been the main reason of the increasing tendency of Zn recoveries observed in the subsequent experiments (shown from Exp. 4–5 to Exp. 8–9 in Figure 8). Assuming that most of the precipitate should contain the thermodynamically most stable solid compounds of zinc in such systems, the temperature dependence of the equilibrium constant of the following precipitation reaction was also examined [9]:

$$5[Zn(NH_3)_4]CO_3(aq) + 17CO_2(g) + 23H_2O = Zn_5(OH)_6(CO_3)_2(s) + 20NH_4HCO_3(aq) \tag{3}$$

and it was found that it slightly decreases with increasing temperature, hence higher Zn recoveries are expected to occur at lower temperatures, which was indeed the case at the lowest temperature (12 °C) studied experimentally as well.

## 4. Experiments on steam distillation

The aim of the third part of our experimental investigations was to study the recovery of zinc from those zinc-laden residual solutions which are left behind after the precipitation procedure by $CO_2$ addition. For this the technique of the so-called steam distillation was chosen and tested. Here, in principle, the decomposition of the zinc ammonia complex can be described by the following reaction:

$$5Zn(NH_3)_4CO_3 + 3H_2O \rightarrow 2ZnCO_3 \cdot 3Zn(OH)_2 + 20NH_3 + 3CO_2 \tag{4}$$

While feeding hot steam into the zinc containing solution, the zinc ammonia complexes, as well as ammonia ($NH_4OH$) and the dissolved ammonium carbonate and hydrocarbonate components would all degrade. As a result, the ammonia ($NH_3$) and carbon dioxide ($CO_2$) gaseous degradation products will leave the system together with the purging water steam.

Here again, for this purpose as well a new home-made simple laboratory apparatus was assembled and the feasibility of steam distillation for the given model solutions were studied in some more experimental trials.

During warming up the solution up to about 90 °C with bubbling through the hot water steam, there was not any noticeable amount of solid precipitates, but as the temperature of the solution reached that value (in about 38 minutes) the solution became opalescent and after about 55 minutes, when also the first samples were taken for chemical analysis, the rate of the zinc precipitation became quite spectaculous. Finally *Figure 9* also clearly shows that the rest of the solution zinc-content remained dissolved after the previous precipitation step (by bubbling $CO_2$ through the solution) could be fully recovered in about 70 minutes by steam distillation. Of course, the ammonia and $CO_2$ driven out together with the hot water steam should concurrently be properly collected, after which the reclaimed and regenerated aqueous ammonia ammonium carbonate can be sent back and utilized again in the primary leaching step in a closed system.

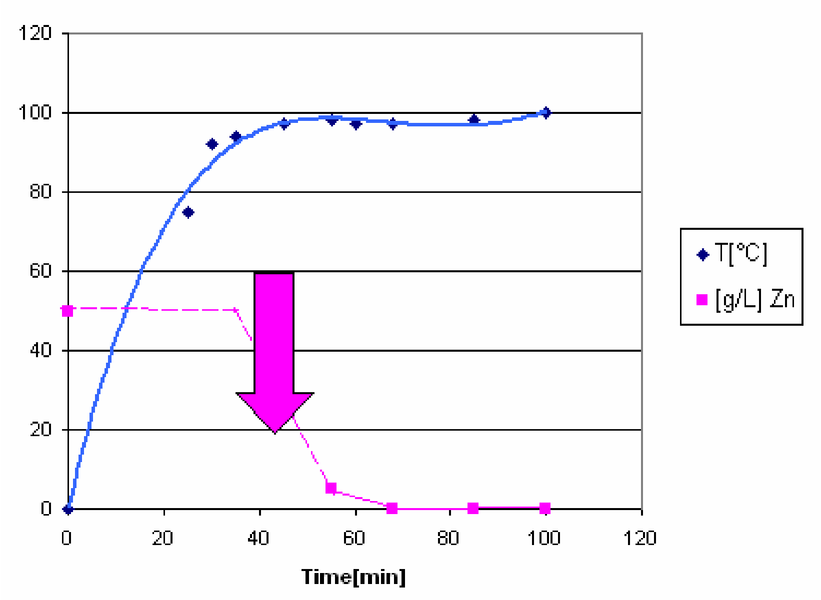

*Figure 9. Progress of zinc precipitation of solid zinc compounds during steam distillation from ammonia ammonium carbonate solutions baren with soluble zinc complexes [the values in g/L concentration show the analyzed Zn-content in the liquid phase]*

## Conclusions

In the course of the three different sets of our laboratory experimental work the major conditions of zinc precipitation from zinc containing aqueous ammonia-ammonium carbonate solutions were examined using zinc baring real liquors obtained by the leach-grinding REDILP-type digestion of some industrial EAF dust samples as well as by testing some model solutions of similar initial composition but without any other slightly soluble contaminating compounds like iron and lead.

At first, the solutions prepared from pure chemicals (so-called model system), as well as the leached liquors obtained from the EAF dust (Bous) REDILP leach-grinding experiments were tested in stirred laboratory precipitation reactors equipped with dosing inlets to supply and dissolve gaseous $CO_2$ as a precipitation agent. As the recovery rates were insufficiently low in both sets of precipitation experiments with carbon-dioxide, the hot water steam distillation technique was also tested to determine its feasibility and efficiency in recovering zinc from such solutions.

In this respect it was proved experimentally that steam distillation is indeed a very efficient technique to induce decomposition of the soluble ammonia complexes of zinc and trigger its precipitation in the form of its most stable insoluble solid zinc carbonate/hydrocarbonate compounds from such aqueous systems. In the same time the water steam drives out part of the dissolved ammonia and $CO_2$ too, which must be recovered in a closed system then can be send back for leaching.

Even though the leaching selectivity of ammonia-ammonium carbonate system is relatively high for dissolving at least part of the zinc content (mostly zincite) from the EAF dust, but our experimental study also revealed the complexity of this approach. However based on the experimental results the presented data could help to design a viable flowsheet of a feasible process to recover zinc, but it is essential that it should be a proper combination of several techniques.

**Acknowledgement**

*The described work was carried out as part of the TÁMOP-4.2.1.B-10/2/KONV-2010-0001 project in the framework of the New Hungarian Development Plan. The realization of this project is supported by the European Union, co-financed by the European Social Fund.*

## References

[1] Antrekowitsch, J.–Antrekowitsch, H.: Dezincing of Steel Scrap – *A solution to the Zinc-Iron Problem in Steel Industry*. BHM 149(1), 28–34., 2004.

[2] Zoz, H.–Kaupp, G.–Ren, H.–Goepel, K.–Naimi-Jamal, M. R.: *Recycling of EAF dust by semi-continuous high kinetic process.* Metall 59(5), 200–203., 2005.

[3] Final Activity Report, Recycling of Electric Arc Furnace (EAF) Dust by Integrated Leach-grinding Process, CRAFT Project COOP-CT-2004-508714. 2007.

[4] Dreisinger, D. B.–Peters, E.–Morgan, G.: *The hydrometallurgical treatment of carbon steel electric furnace dusts by the UBC-Chaparral process*. Hydrometallurgy (2), 137–152., 1990.

[5] Prado, F. G.: High Purity Zinc Oxide from a *Wide Range of Industrial Residues*. Second International Symposium- Recycling of Metals and Engineered Materials; Edited by Jan H.L. van Linden, Donald L. Stewart, Jr., and Yogeshwar Sahai; The Minerals, Metals & Materials Society, 529–535., 1990.

[6] Andersson S.O.S: Meixner, M. J.: *Ammoniakalischer MAR-Prozeß – Wiedergewinnung von Kupfer, Nickel und Zink aus ammoniakalisch gelaugten Neutralisationsrückständen*. Aufbereitungs-Technik (5), 264–268., 1979.

[7] Wendt, W. J.: *Ammonia, Ammonium Carbonate Leaching of Low grade Zinc Ores.* Engineering and Mining Journal 154(9), 84–90., 1953.

[8] Üveges, V.–Gábor Mucsi, G.–Bokányi, L.: Experimental investigation of leach-grinding process for the recycling of EAF dust – MicroCad International Scientific Conference, 2008, 93–98.

[9] Török, T. I.: *Chemical metallurgical techniques applied in some precipitation and surface engineering systems*. HAS Doctoral Dissertation, 2006, 30.

University of Miskolc, Department of Research Management and International Relations
Responsible Publisher: Prof. Dr. Mihály Dobróka prorector
Published by the Miskolc University Press under leadership of Erzsébet Burmeister
Responsible for duplication: Erzsébet Pásztor
Miskolc-Egyetemváros, 2013
Copies: 150
TU – 38 –2013 – ME HU ISSN 2063-6792